AIMS Mathematics, 10(10): 23084–23135.
DOI: 10.3934/math.20251025
Received: 27 July 2025
Revised: 05 September 2025
Accepted: 18 September 2025
Published: 11 October 2025

https://www.aimspress.com/journal/Math

Research article

A comprehensive review on artificial neural network techniques (Levenberg–Marquardt, Bayesian regularization, scaled conjugate gradient) for magnetohydrodynamic hybrid nanofluid flow with bio-convection and heat sources

Sohaib Abdal[1,†], Adnan Ashique[2], Usman Afzal[2], Maddina Dinesh Kumar[1], Khalid Masood[3,*] and Nehad Ali Shah[2,†]

[1] Department of Mathematical Sciences, Saveetha School of Engineering, SIMATS, Chennai, Tamilnadu 602105, India
[2] Department of Mechanical Engineering, Sejong University, Seoul 05006, South Korea
[3] Department of Mathematics and Statistics, College of Science, Imam Mohammad Ibn Saud Islamic University (IMSIU), Riyadh 11623, Saudi Arabia
† Sohaib Abdal and Nehad Ali Shah contributed equally to this work and are co-first authors

* **Correspondence:** Email: kmaali@imamu.edu.sa.

Abstract: Integration of artificial intelligence into computational fluid dynamics has significantly enhanced the simulation of complex transport phenomena. This review presents a detailed analysis of artificial neural network (ANN) techniques, namely Levenberg Marquardt (LM), Bayesian Regularization (BR), and Scaled Conjugate Gradient (SCG), in the simulation of magnetohydrodynamic (MHD) hybrid nanofluid flows with bio-convection and internal heat generation. Such flows are characterized by strong nonlinearities arising from the synergistic interaction of magnetic forces, nanoparticle-particle interactions, convective effects caused by microorganisms, and heat gradients. Traditional numerical methods, though well-refined, typically face convergence issues, computational costs, and adaptability to highly nonlinear cases. ANN-based models, on the other hand, show remarkable characteristics toward the approximation of intricate physical correlations with enhanced convergence and generalization. This review discusses, in a detailed manner, the theoretical basis, training behavior, prediction accuracy, and computational efficiency of LM, BR, and SCG algorithms in maintaining critical fluid properties like velocity,

temperature, and concentration. Special focus is given to the role played by bio-convection in enhancing transport properties and to how ANN techniques effectively model these dynamics with minimal residual error and computational intensity. A comparative study highlights the applicability and uniformity of such neural network algorithms in advanced heat and mass transfer operations with MHD hybrid nanofluids.

Keywords: hybrid nanofluid; magnetohydrodynamics; artificial neural networks (ANNs); bio-convection
Mathematics Subject Classification: 70G10, 76A05, 76R05, 80A05

1. Introduction

Hybrid nanofluids are composed of more than one type of nanoparticle, designed to enhance the thermophysical properties of the base fluid. The nature of the mono-nanofluids may be modified by altering the level or fraction of the nanoparticles. Mono-component nanoliquids, on the other hand, show stable thermophysical properties in a limited scale, with only one nanoparticle type, either nonmetallic or metallic. Hybrid nano-fluids were developed in the last few years to overcome thermal transfer and thermophysical properties of fluids in which base fluid is mixed with two different types of nanofluids. Hybrid nanofluids have been shown to improve the performance of mono-nanoliquids in relation to thermal dissipation, also showing higher thermal conductivity and enhanced thermophysical characteristics than traditional fluids. Studies suggests that the heat distribution rate of a hybrid nanofluid-based heat transfer system is significantly better compared to conventional nanofluid flows, despite the effects of thermal radiations, heat generation, and industrial activity. The miniaturization of components and rapid advances in fabrication techniques have led to significantly higher heat fluxes, posing serious challenges for conventional cooling technologies. The main objective of using a hybrid nanofluid (HNF) is to improve the thermal performance of various engineering and industrial processes such as sheet fabrication and rubber processing, among other modern applications. In extrusion process, the quality of the final product depends on heat and mass transfer. Scientists have been increasingly interested in the application of hybrid nanofluids in areas such as medicine, aerospace, ship building, microstructural, and mechanical engineering, defense, and propulsion. Alkuhayli [1] investigated the effects of nanoparticle volume fraction, thermal radiation, and magnetic field strength in hybrid nanofluid flows, showing that an increase in such parameters raised fluid velocity and temperature. Venkateswarlu et al. [2] studied $CuTiO_2 / H_2O$ hybrid nanofluids and showed that suspensions containing multiple types of nanoparticles lead to enhanced heat transfer in comparison to single-component nanofluids and viscous fluids. In a study carried out by Ontela et al. [3], $CuTiO_2 / H_2O$ hybrid nanofluids were investigated, and their high thermal efficiency was confirmed under different nanoparticle concentration. As part of their analysis, Atashafrooz et al. [4] used numerical methods and similarity transformations to the governing equations of hybrid nanofluid heat transfer, highlighting the significant role of thermal radiation and inclination angle of the magnetic field in achieving optimal thermal transport. Al-Kouz et al. [5] investigated the thermal efficiency of a radiative ternary fix/Nf mixed nano fluid consisting of Al_2O_3, TiO_2 and Ag nanoparticle coatings around a vertical magnetized cylinder. Awan et al. [6] conducted a numerical study of heat transfer in Ellis hybrid nanofluid flow, considering with the effects of a stretching cylinder, magnetic fields, Darcy-Forchheimer drag, and nonlinear thermal radiation.

Qayyum et al. [7] investigated chemical reactions and nonlinear thermal radiation in hybrid nanofluid, finding that the heat transfer rate increases during blood flow. Sandeep et al. [8] showed that hybrid nanofluids have better heat transfer performance than traditional nanofluids when flowing over a nonlinearly extending surface in presence of the radiation effects. Reddy et al. [9] achieved an extensive examination of the heat and mass transfer characteristics of a hybrid nanofluid consisting Al_2O_3 and TiO_2 suspended in water over a stretching /shrinking sheet, accounting for slip effects, chemical reactions, suction, and thermal radiations. Farooq et al. [10] examined the radiative flow and convective heat transfer of magnetized hybrid nanofluids, namely $Fe_3O_4TiO_2 / TO$ and $CuTiO_2 / TO$, over double rotating discs using the Cattaneo-Hristov heat flux. Li et al. [11] studied the impact of an externally applied magnetic field on the heat and mass transfer behavior of hybrid nanofluids, considering the impacts of chemical reactions and the concentration of pollutants. Ouyang et al. [12] analyzed unsteady hybrid nanofluid flow in porous channels with suction/injection, unsteadiness, and thermal stratification, finding that copper nanoparticles can significantly delay boundary-layer separation, thereby enhancing convective heat transfer. In a study conducted by Algehyne et al. [13], it was found that higher magnitudes and steeper gradients of the magnetic fields result in slower fluid flow with simultaneously increasing thermal intervals. Gul et al. [14] conducted a comprehensive natural convection analysis in porous square cavities filled with $CuAl_2O_3$/water hybrid nanofluids. The results revealed that higher nanoparticle volume fractions, Rayleigh numbers and Darcy numbers significantly enhance convective heat transfer rates. Paul et al. [15] analyzed $CuAl_2O_3$/water hybrid nanofluids in porous media and showed significantly improved thermal conductivity in comparison to both conventional fluids and single-component nanofluids, with heat flow being additionally regulated by applied magnetic fields. Ismail and Gururaj [16] investigated the impact of nanoparticle volume fraction and medium porosity in hybrid nanofluid-filled cavities, showing that higher nanoparticle levels substantially and optimal porosity levels boost convective heat transfer and modify velocity distributions. Yang et al. [17] studied hybrid nanofluids containing Cu, Al_2O_3, Co, Au, and ZrO_2 nanoparticles in water or paraffin over stretched surfaces in a porous medium. Their results indicated significant improvements in skin friction, velocity distribution, and thermo-hydraulic performance with increasing nanoparticle concentration, porosity, and magnetic field intensity. Memon et al. [18] conducted an analytical investigation of magnetohydrodynamic (MHD) hybrid nanofluid flow in porous walls using on numerical techniques such as Runge-Kutta integration, the bvp4c solver, and shooting implementing techniques, concluding that stronger magnetic fields and higher nanofluid concentrations significantly influence momentum and heat transport. Sohut et al. [19] conducted a study on hybrid nanofluid flow past inclined cylinders, demonstrating that the synergistic action of buoyancy forces, magnetic fields, and thermal radiations enhance heat transfer while reducing drag compared to standard fluids. Rafique et al. [20] investigated the influence of variable thermal conductivity, viscosity, and mass suction on hybrid nanofluids performance, showing significant changes in both velocity and temperature profiles. Rasool et al. [21] carried out a systematic study of the Falkner-Skan flow of hybrid nonpositive fluids in porous media by incorporating the effect of Joule heating and Darcy-Forchheimer drag and found considerable improvements in the convective heat transfer as a result. Using non-Newtonian fluid systems, Sajid et al. [22] conducted an analytical analysis of the tetra-hybrid nanofluid models, explaining that these models have a significant chance of increasing the heat and mass transfer in technological processes dealing with solar energy. Sarkar and Das [23] conducted an in-depth study of hybrid nanofluid flow that considered the effect of activation energy and chemical reaction dynamics. Results showed that an increase in activation energy significantly increases both heat and mass transport rates, while exothermic reactions reduce both rates.

Guo et al. [24], MHD hybrid nanofluid flows and determined that the use of magnetic fields leads to a decrease in flow velocity, while increasing the thermal profiles and Nusselt numbers. Abd-Elmonem et al. [25] investigated MHD hybrid nanofluid heat transfer under different magnitudes of the magnetic field and proved that existence of a trade-off between thermal enhancement and hydrodynamic damping. Haq et al. [26] investigated the dynamics of hybrid nanofluid suspensions with three different types of nanoparticles and determined that such systems have increased capability of heat transfer compared to binary mixtures. In the study by Reddy et al. [25], Williamson hybrid nanofluid stagnation-point flow was analyzed, having been noted that high porosity relates to high flow velocity, and thermal radiation enhances temperature profiles. An analysis on $CuAl_2O_3$/water hybrid nanofluids with both homogeneous and heterogeneous reactions, conducted by Ahmed [27], unveiled the existence of numerous solution pathways and the prevalence of thermophoretic deposition through competitive Brownian diffusion processes. Manigandan et al. [28] conducted a study of $CuTiO_2$/water hybrid nanofluid flow in an inclined plate with combined incorporation of chemical reactions and viscous dissipation in the MHD scenario. Khalatbari et al. [29] conducted a critical study of hybrid nanofluids and proved that the combination of various nanoparticle types in a base liquid can lead to up to 35% improvement in heat transfer efficiency due to better thermal conductivity and stability. An analysis of convective Marangoni flow with hybrid nanofluids flowing between infinitely sized disks was conducted by Abbas et al. [30] including both thermophoresis and electrophoresis. Marulasiddeshi et al. [31] conducted a study on CuO and Al_2O_3 hybrid nanofluids in circular tubes and recorded significant improvements in the Nusselt number and thermal performance factor at different inlet temperatures. Mahmood et al. [32] carried out an analysis of MHD stagnation-point flow of Al_2O_3-Cu/water hybrid nanofluid over a stretching sheet and showed that the Yamada-Ota thermal conductivity model improved heat transfer rates compared to the other models. Hayat et al. [33] examined the peristaltic transport behavior of an MHD hybrid nanofluid via porous media and showed that increased nanoparticle concentration yields significantly higher rates of heat transfer. In a study by Alharbi et al. [34], the phenomena of thin-film flow of hybrid nanofluid ($CuAl_2O_3$ /water) over an inclined rotating disk was investigated; and the enhanced thermal performance provided important implications on solar water-heating technology. An analytical report of a hybrid nanofluid flow over shrinking surfaces was conducted by Saleem et al. [35]; authors examined the effects of a lack of thermal radiation and viscous dissipation and found that both results in a significant increase in the fluid temperature during its flow. Abbas et al. [36] carried out a comprehensive exhaustive study on engine oil-based hybrid nanofluids in porous inclined cavities using MHD conditions, showing that the higher the Hartmann numbers and thermal radiation parameters, the higher the heat flux rates. In Elfiano et al. [37], a study was carried out on the mixed convection boundary layer flow of hybrid nanofluids over a vertical flat plate; results showed that both higher nanoparticle volume fractions and buoyancy forces greatly enhanced heat diffusion compared with single-component fluids. The unsteady MHD flow of Fe_3O_4MWCNT /water hybrid nanofluids between rotating disks was examined in Tulu et al. [38], where it was shown that velocity and thermal profiles significantly varied under the influence of magnetic field strength and viscous dissipation, and that the effect of hybrid nanofluid increased heat transfer by a large margin (up to 20%). Rehman et al. [39] analyzed stretch-dependent MHD Casson flow of hybrid nanofluids over stretching bodies and observed that the magnetic parameter and nanoparticle concentrations induce substantial increases in Nusselt numbers and general efficiency of heat transfer. Mishra et al. [40] investigated the enhanced heat transfer performance of a water-based hybrid nanofluid consisting of Al_2O_3 and Cu nanoparticles flowing through a rotating vertical cone; the flow of the hybrid nanofluid was

found to be highly enhanced by magnetic fields and thermal radiation. Choudhary et al. [41] investigated the importance of unstable MHD hybrid nano-fluid flow around a nonlinear stretchable porous sheet for thermal radiation and gyrotactic microorganism applications. Using a 3D stretching sheet, Ramana et al. [42] evaluated out the impacts of radiation absorption, Forchheimer number, porosity, magnetic field, and aligned magnetic field on the circulation and heat exchange of a hybrid nanofluid. Muhammad Raza Shah Naqvi et al. [43] analyzed the entropy production involved in the flow of GO-Fe_3O_4/water hybrid nanofluid in the presence of magnetic fields, showing significant thermal transfer enhancement. Madhu et al. [44] estimated the effect of linear, nonlinear, and quadratic thermal radiation on a hybrid nanofluid flow in a cylinder and concluded that the quadratic radiation produces minimum temperature profiles. Bani-Fwaz et al. [45] investigated the thermal properties of the hybrid nanofluid under the influence of heat sources and solar radiation and noted the significant enhancement of the heat transfer parameters. The Casson hybrid nanofluid ($AgGo$) flow was investigated by Mohanave [46] in a stenosed artery, where he found that increased values of Darcy number and Grashof parameter contributed to increasing the velocity of the fluid. Thirumalaisamy et al. [47] conducted a buoyancy-based analysis of MHD hybrid nanofluid inside a partially heated porous square cavity, where an increase in the porous parameters and nanoparticle concentration significantly increased total heat transfer. Anup Kumar et al. [48] considered the dynamics of Jeffrey hybrid nanofluid flow involving gyrotactic micro-organism in porous media in a solar thermal collector; results revealed that increasing Darcy and Forchheimer numbers significantly increase the thermal profiles and Nusselt numbers. Almeshaal [49] investigated 3D convective flow through a bi-truncated pyramid and reported paralleled enhancement in heat transfer at higher Rayleigh numbers and higher nanoparticles concentrations. Hai et al. [50] conducted an analytical study employing a computational intelligence framework that integrates machine learning and multi-objective optimization to determine the best working conditions of $Go/Fe_3O_4/TiO_2$ ternary hybrid nanofluids, demonstrating major improvements in several measures of thermal performance. Hassaan [51] carried out an experimental investigation of Fe_3O_4MWCNT /water hybrid nanofluid in a shell and tube heat exchanger and recorded an increase of up to 35% in Nusselt number and a better performance of the heat exchanger as compared to distilled water.

Electrically conducting fluids (plasmas, liquid metals, and ionized gases) can have different properties when in the presence of magnetic fields; and this is the basis of the interdisciplinary research area of physics and engineering involving magnetohydrodynamics. This discipline borrows concepts from electromagnetism and fluid dynamics to explain the impact of magnetic forces on such conducting fluids, which in turn explains the velocity and conductivity of the fluid. Characteristics of nanofluid flows gain an entirely new level of complexity when MHD effects, activated due to the use of magnetic fields, become involved and alter the fluid dynamics as well as the thermophysical properties. The MHD combines a fluid, magnetic field, and associated phenomena and examines them all together, scrutinizing their evolution. The flow behavior described by MHD has been the subject of numerous applied and theoretical studies due to its wide range of industrial applications. This field has gained prominence because of its relevance in areas such as electric propulsion systems, aircraft design, and nuclear reactor cooling designs. MHD is an emerging as a potential area of research in biological engineering. In a range of physical, geothermal, and industrial fields, MHD flow has also resulted in a large body of experimental and theoretical research work. It is widely accepted that the interest on MHD flows related to heat relates to the commercial applications in which they may be used, including nuclear reactor cooling systems, electric propulsion of expanding space, aircrafts, crystal growing in liquids, and the microelectronic devices. Khan et al. [52] conducted a detailed study of MHD hybrid nanofluid flow on porous stretching sheet, considering various slip boundary conditions, thermal

radiation phenomenon, and internal heat source term; results showed that hybrid nanofluid formulations are very effective in increasing both heat and mass transfer rates compared to using single-component nanofluids. Prajapati and Meher [53] studied revealed the effect of base-fluid constituency, i.e., water, ethylene glycol, and combinations including copper and aluminum oxide nanoparticle; it was found that optimum proportions of base-fluid components can greatly increase heat transmission in MHD flows. Sadighi et al. [54] studied the combined impacts of an imposed magnetic field, the power-law exponent of concentration, and homogeneous-heterogeneous reactions on the interaction with nanofluid-boundary layer dynamics; results indicated that bulk pressure and reaction dynamics significantly influence velocity, temperature, and concentration gradients. Nazeer et al. [55] compared the thermal performance of water-based nanofluids and hybrid nanofluids composed of titanium alloy and aluminum alloy within a thermally heated square cavity influenced by a magnetic field. Madan Kumar et al. [56] studied the effects of chemical reactions along with Soret and Dufour effects on MHD dissipative Williamson nanofluids flowing over a slippery stretching sheet in a porous media. Asghar et al. [57] numerically investigated the influence of MHD, mixed convection, heat generation/absorption, and velocity slip on magnetized nanofluids flow over a shrinking sheet. Mechai et al. [58] assessed nanofluids in a curved enclosure and concluded that an increased Hartmann number reduces heat transfer, whereas an increased Rayleigh number increases heat transfer. Rothan [59] conducted an analysis of nanofluid flow in a porous container and found that the use of nanoparticles results in a 41.42% increase in heat transmission. Vinodhini and Prasad [60] studied an MHD convective nanofluid flow in a rectangular enclosure based on the Buongiorno model, showing that Brownian motion and thermophoretic movement play important roles in the distributions of temperature and concentration. Kumar et al. [61] conducted an analytical research concerning MHD stagnation-point flow with a negative activation energy; the researchers found that skin friction and the Sherwood number increases with increasing unsteadiness. A three-dimensional MHD nanofluid flow analysis was carried by Tarakaramu et al. [62] that included the activation energy and confirmed that the concentration of nanoparticles and mass transfer rate increase with increasing activation energy. Jayanthi and Niranjan [63] studied the flow of MHD nanofluid over a vertical surface, including Joule heating and viscous heating, explaining that an increase in the Schmidt number would improve the temperature and concentration profiles. Vijay and Sharma [64] carried out an elaborate study on MHD hybrid nanofluid flow on a rotating disk with deceleration considering Soret and Dufour effects and explaining how deceleration disks affect the velocity profiles of the fluid. Aruna and Niranjan [65] examined the processes of a micropolar hybrid nanofluid flow; they noticed that the fluid mobility markedly improved due to the presence of electromagnetic forces and mixture convection. An extensive entropy generation analysis of MHD electroosmotic peristaltic transport of nanofluids was carried out by Reddy et al. [66] by considering Ohmic heating, Hall current, and viscosity with temperature, while reviewing thermal irreversibility and pumping mechanisms efficiency. Within ciliary navy carpets, Ijaz et al. [67] discussed the impacts of the dispersion of electroosmotic nanofluids in microchannels and discovered that surface-based oscillation assists the level of nanoparticle dispersion and mixing of biofluids. In Gandhi et al. [68], an analytical analysis was performed to study the electromagnetohydrodynamic centrifugal behavior of non-Newtonian nanofluid blood flow travelling into a stenotic disease artery with an irregular circumference and an aneurysm. Raizah et al. [69] investigated the MHD flow in a gyrating channel of a hybrid nanofluid of copper suspension in alumina on water, taking into consideration the coupled Dufour-Soret effect and the dynamics of chemical reactions. Prashanth and Rao [70] performed an analytical analysis of the MHD flow of nanofluids on a variable stretching sheet, explicitly considering Soret and Dufour effects in addition to the effect of chemical reactions, thermal radiation, and variable viscosity; their numerical

results showed that a high value of Soret number increases temperature profiles, but a high value of Dufour number reduces thermal gradients. Maheswari et al. [71] conducted an analytical analysis of the hybrid nanofluid flow on a slender needle in an MHD environment; results showed that an increment in the thermophoretic parameter leads to the decrease of both temperature and concentration profiles. In Mirza et al. [72], an analysis study on permeable media whose flow was exposed to heat was performed, and it was found that increased medium permeability and larger Soret numbers led to a significant increase in flow velocity. Priyadharsini and Sheremet [73] performed a numerical study of bioconvective blood flow, which showed that increased thermophoresis and Brownian parameter led to a greater heat transfer efficiency in general. Das et al. [74] studied thermophoretic deposition in MHD flow over a vertical plate and found that with increasing thermophoretic parameters, fluid velocity, temperature, and concentration fields decrease.

MHD nanofluid flows were thoroughly examined by Hasanuzzaman et al. [75]; findings revealed that increased Eckert number accelerates the increase of temperature and the velocity of the fluid; also, suction parameters reduce velocity, concentration, and temperature distributions. Sahu et al. [76] studied an unsteady MHD flow over an infinitely deep vertical plate in a porous environment, considering features related to thermal stratification, chemical reactions, radiation, and thermal sources, and showing that the straining effect strongly suppresses the velocity and temperature profiles. Conducting a formal analysis of the MHD flow through porous media with nonlinear thermal radiation and density changes, Dutta and Kalita [77] revealed that the given phenomena allow generating a more efficient heat transfer, whereas the use of suction ensures better flow stability. Maranna et al. [78], analyzed MHD biviscous Bingham flow in the context of tetra-nanofluids by incorporating chemical reactions and heat radiation. It was found that the fluid velocity reduced with an increase in strength of the magnetic field, and that the pattern of temperature growth and concentration also increased at the same time. Fetecau et al. [79] analyzed the MHD flows of second-grade fluids through porous media by showing that the introduction of magnetic fields and an increased porous resistance slow down the flow of fluids by increasing the rate at which the steady-state is reached. Negi et al. [80] performed with an analysis of the flow of water-based ferrofluids inside a horizontally located channel, where the combination of MHD forcing enhanced velocity and heat transfer closest to the upper channel wall, is supported by the presence of the magnetic field and heating of the channel walls. Ilias et al. [81] conducted an analysis of the MHD natural convection within an octagon-shaped cavity containing nano-encapsulated phase-change material and porous medium; results showed that increased Reynolds and Darcy numbers will contribute to higher heat transfer, while and a strong magnetic field will reduce the intensity of convection. A model of the passage of electromagnetohydrodynamic micropolar fluid through a porous membrane made up of cylindrical particles was developed by Yadav and Srivastava [82]. Rajakumar Komaravolu et al. [83] examined the interactions of Dufour and Soret diffusion on MHD convective flow of fluids moving to the top of a vertical porous plate. Deka and Choudhury [84] conducted an investigation of Soret and Dufour effects on MHD flow between wavy and flat walls, as they are relevant in mediating heat sources and chemical reaction rates. Aich et al. [85] conducted a study of a stagnation-point of a second-grade fluid subjected to the double-diffusive MHD condition and used the non-Darcy porous interior to parameterize their estimations, considering both the Soret and Dufour effects. Pan and Ni [86] conducted an analytical examination of liquid metal flow in an open channel that is exposed to a transverse magnetic field, showing that scaling laws are relevant in terms of film thickness and the three-dimensional development of a free surface.

Bioconvection refers to the collective motion of a suspension of self-propelled microorganisms. It occurs when bacterial entities or biological solutions are combined with fluids. This is mostly caused

by diluted fluids, whereby bacterial organisms have the ability to undergo locomotion; thus instability occurs as a result of density changes. Bioconvection within the framework of biological sciences has been extensively studied and is of great importance in the field of bio-microsystems. Additionally, another possible use of the bioconvection concept may relate to the oil remediation process, in which its sustainability is enhanced by incorporating microorganisms and nutrients, including vitamins, proteins, and fibers, into the layers of the oil reservoir to improve permeability and facilitate gaseous or liquid diffusion. As such, a deep understanding of how bioconvection works along with other physical processes is of paramount importance. An important tool is physical models, which are more applicable and attractive by incorporating the properties of non-Newtonian fluids. Additional physical factors, such as nonlinear thermal radiation, multi-slip circumstances, and magnetic fields, are included to make the physical model more realistic. Li et al. [87] conducted a study of the bioconvection-induced behavior of Sutterby nanofluid with magnetic fields, focusing on how the motion of microorganisms improves thermal performance in bioprocessing and biosensor applications. Liu et al. [88] investigated the Casson nanofluid flow over stretching surfaces and showed that a change in slip conditions and Peclet numbers affects microorganism density and the rate of heat transfer. Dharmaiah et al. [89] assessed hybrid nanofluid bioconvection and revealed an increased total heat transfer effectiveness due to the influence of nanoparticle-microorganism interactions. Tlili et al. [90] evaluated the enhanced thermal conductivity of nanofluids by using non-Newtonian fluid, bioconvection, and external heat, focusing on its use in renewable energy storage systems. Aljaloud et al. [91] investigated bioconvective flow of Cross nanofluid in a stretching cylinder with activation energy and second-order slip factors. Makkar et al. [92] examined how magnetized nanoparticles affect the bioconvective Casson fluid flows and revealed that the change of the magnitude of the magnetic field and the bioconvection Rayleigh numbers significantly change microorganism accumulations and flow regimes. Patil and Benawadi [93], Eyring-Powell nanofluids were examined with bioconvection Lewis numbers, leading to the conclusion that high nanoparticle diffusion and high microorganism density play a massive role in increasing entropy generation and altering the microorganism concentration profiles. Hussain et al. [94] conducted a detailed investigation on the aspects of inclined magnetization in hybrid nanofluids, explaining that high values of thermal Biot numbers play a crucial role in raising heat transfer rates and shear stress distributions. Ali et al. [95] investigated magnetized Sutterby nanofluids, including thermophoresis and Brownian motion, and showed that thermophoretic forces were able to induce higher liquid temperatures, whereas higher Peclet numbers lead to a reduction in the density of microbe populations. Hussain et al. [96] examined Eyring bioconvective flows under magnetic conditions, stating that similar thermophoretic effects were observed on temperature profiles and distribution of microorganisms. Kopp and Yanovsky [97] conducted an analysis of the phenomenon of gravity modulation of gyrotactic bioconvective flow through porous media and revealed that modulation substantially boosts heat transport mechanisms. Rehman et al. [98] examined the effect of the volume fraction of nanoparticles, Knudsen number, and Peclet number-driven bioconvection on the velocity and density of microorganisms in the context of a Darcy-Forchheimer nanofluid. Nihaal et al. [99] modeled porous-medium resistance and showed that an amplified value of Forchheimer numbers increases the resistance of the flow and decreases the velocity of the fluid near to the stretching sheet. Alqurashi et al. [100] studied the micro-pole nanofluid flow over oscillating surfaces, considering the combined effects of melting heat, thermal radiation, and micro dynamics of motile microorganisms in velocity and thermal profiles. The study of Prasannakumara et al. [101] involved bioconvective nanofluid circulation over exponentially stretched sheets in terms of thermophoretic particle deposition, in which the higher the porosity of the medium, the lower the mass flow velocity and skin friction, with solid volume fractions associated with higher

thermal distribution. Chu et al. [102] analyzed bioconvection in tangent hyperbolic fluids, involving the dynamics of the double-diffusive magnetized bioconvection, considering activation energy and thermophoretic forces interaction with Brownian movements. Kolsi et al. [103] performed a study on bioconvective Jeffrey fluid flow on an oscillating, stretched bidirectional surface, considering thermal radiation and changing viscosity impacts. Peter et al. [104] investigated the behavior of MHD bioconvective Eyring Powell fluid flow and showed that a stronger magnetic field and porous media greatly increase microbial diffusion. Khan et al. [105] conducted an in-depth study on the phenomenon of MHD bioconvective flow, considering a nanofluid that comprises gyrotactic microorganisms flowing through a porous medium and incorporating thermal radiation and chemical reaction; their results depict that more intense magnetic fields will reduce the velocity of the fluid flow and at the same time increase the temperature distributions. Also elevated nondimensional Soret numbers increase the boundary layer of concentrations. Ibrahim and Gizewu [106] investigated entropy production under bioconvective flow in nanofluids over surfaces with curved stretchiness and explained that the synergistic impact of Soret and Dufour movements, as well as surface deformation, was sufficient in enhancing thermodynamic irreversibility. Das et al. [107] analyzed the thermo-solutal Marangoni convection in Powell-Eyring nanofluids and showed that surface-tension gradients promote the transfer of mass as they inhibit the movement of heat and reduce gradients of microorganism density. An investigation of bioconvective flow of nanofluid Casson with toxic reactions and thermal effect by Arun et al. [108] highlighted the crosslinking of temperature regimens and reaction encounters to carve the circulation design. Shah et al. [109] studied the micropolar condition of nanomaterial flow, where motile microorganisms were present in the flow of the material and the paramagnetic field under MHD conditions, and discovered that fluctuations in the strength of the magnetic field and porosity of the medium lead to the decrease of radial velocity.

Over the past few years, many investigations about the uses of artificial neural networks (ANN) in thermodynamics have been carried out. Artificial neural networks (ANNs) can learn proficiently through self-adaptation of incoming data, which is enforced through the provision of learning algorithms. Therefore, they are a very useful tool in modeling statistics of nonlinear data. Levenberg-Marquardt backpropagation algorithm is an approach to train the network. The training process automatically stops when the mean square error (MSE) of the validation samples starts to increase, as it means that no further generalization can be achieved. The use of the Levenberg-Marquardt technique coupled with the backpropagation method has enabled scholars to venture into the realms of artificial neural networks. Neural networks have wide uses in different applications, such as signal processing, identity identification, prediction, and security, among others. The use of neural networks will only increase in the future due to the development of fast training techniques and the improvement of processing time, which will enable them to be used to solve complex technical problems requiring large computing power. The most unique characteristics of a neural network algorithm is its adaptive learning, flexibility, generalization potential, and systematic organization in terms of data storage. It is also true that neural networks have the property of extending and parallel processing, which ensures efficiency of operation and non-severe loss of performance in the occurrence of network loss. To build an ANN-BLMM (Artificial Neural Network with Bayesian Levenberg–Marquardt Method), 100 input grids on a matrix [0, 1] are created as a reference dataset. Data will be divided into 10% (TT) training test, 10% (TR) training, and 80% (VL) randomly assigned to validation. The TR data is produced in order to come up with the estimated solution, but the VL data is used to design the neural network with a merit criterion (MSE). The TT information is used to estimate the performance factor (PF) of impartial participation. In this flow prediction task, an ANN-BLMM is run using the TT data. Jakeer et al. [110] executed a comprehensive investigation concerning the heat transfer characteristics of

nanofluids within star-shaped enclosures, elucidating that ANN models possess the capability to precisely forecast temperature and flow distributions under diverse nanoparticle concentrations and boundary conditions. Basu et al. [111] carried out an analytical study on the derivation of thermophysical properties of nanofluids, specifically thermal conductivity and specific heat capacity, through the utilization of ANN frameworks, achieving correlation coefficients (R-values) higher than 0.95. Alotaibi et al. [112] engaged in an analytical investigation of nanofluid flow dynamics between inclined cylinders for solar applications, employing ANN frameworks to optimize predictions of Nusselt numbers and geometrical configurations. Shamshuddin et al. [113] analyzed ethylene-glycol-based Fe_3O_4 and MoS_2 nanofluids within porous cylindrical annuli, demonstrating through ANN-assisted evaluations that Fe_3O_4 exhibits superior convective heat transfer rates in comparison to MoS_2. Hudha et al. [114] conducted an analytical research of the MHD mixed convection in triangular cavities with the prediction of heat and mass transfer considering different magnetic field inclination angles, Reynolds number, and nanoparticle concentrations, based on artificial neural networks. In an analytical study of double-diffusive mixed convection in trapezoidal enclosures, conducted by Prince et al. [115], it was shown that ANN models achieve a prediction accuracy of more than 97% under a range of operational conditions. Chinnasamy et al. [116] introduced the artificial neural network model for studying the peristaltic transport phenomena of Sutterby nanofluid flow in a tapered inclined channel subjected to MHD force. Aljuaydi et al. [117] applied the concept of artificial neural networks to study complex phenomena of nanofluids under different states of magnetic fields and the effects of thermal radiation. To increase the predictive accuracy of nanofluid bioconvective models, Shah et al. [118] established a Levenberg-Marquardt backpropagation neural network approach. Kaswan et al. [119] applied back-propagated neural networks to observe the phenomenon of magneto-cross-bioconvection in nanofluids containing gyrotactic microorganisms and activation energy. Yaseen et al. [120] evaluated the transport processes of a hybrid bio-nanofluid in flat plates, wedges, and cones and clarified the geometrical configuration and density of the microorganisms on flow stability and thermal exchange, which is of great interest to microbial-enhanced oil recovery and architecture cooling. Qu et al. [121] utilized ANNS to model the thermal properties of a WO_3-CuO (50:50)/water-based hybrid nanofluid. Borode et al. [122] conducted an extensive study to analyze the use of ANNs to model thermophysical properties of hybrid nanofluids, showing that the ANN methodology is much more effective in predicting viscosity, thermophysical properties, and electrical conductivity than traditional response surface methods. Rawat et al. [123] used fuzzy particle swarm optimization combined with ANNs to maximize the heat transfer of magnetized, radiative ternary nanofluid flow, which indicates the importance of hybrid methods of computation.

Recent advances in scientific machine learning have introduced Physics-Informed Neural Networks (PINNs), where governing physical equations are directly incorporated into the learning process. Cai et al. [124] conducted a pioneering work focusing on how PINNs approach forward and inverse fluid mechanics problems with physical integrity. Zhao et al. [125] subsequently extended this perspective by demonstrating that PINNs might be employed to solve turbulence, multiphase flows, and other nonlinear transport phenomena. Ren et al. [126], gave a methodological summary of recent developments in PINNs, including adaptive optimization and domain decomposition, which enhance convergence and scalability for fluid systems of greater complexity. Operator learning platforms, Deep Nets, and Fourier neural operators have, in the meantime, been presented to learn mappings in function space. Goswami et al. [127] showed that such operators can serve as powerful surrogates of parameterized PDE solvers and can accelerate fluid simulations considerably. In a very recent contribution, Howard et al. [128] presented a stacked network approach that combines PINNs with learning operators for multiphysics accuracy improvement. Such advancements complement

conventional ANN methodologies by adding physical laws, improved robustness, and reduced data dependency in fluid flow simulation. Meng et al. [129] presented an interesting neural network solution to the reverse spectral problem with insufficient information, demonstrating the efficacy of ANNs in solving ill-posed problems. Zhuang et al. [130] developed a robust neural network model for reverse dispersion problems with contaminated data, proving that ANN models could maintain their dependability even in the presence of noisy inputs. Xiao et al. [131] showed how ANNs can accurately depict complex network behaviors by figuring out the local manifold symmetry of nonlinear dynamics using neural ordinary differential equations. Giudici [132] highlighted the significance of creating trustworthy statistical criteria for safe machine learning, pointing out that recent developments in artificial intelligence have heightened global discussions on safety and risk.

Despite significant progress in analytical and numerical simulation of MHD hybrid nanofluid flows, specifically those involving bioconvection and internal heat sources, the application of data-driven and intelligent computational paradigms remains underdeveloped. Conventional numerical solvers, although robust, are likely to encounter challenges in when facing high nonlinearity, coupling effects, and computational costs of such complex physical systems. Artificial Neural Networks (ANNs), with the ability to approximate nonlinear functions as well as learning from pattern data, offer a promising alternative to conventional techniques. However, systematic investigations of various ANN training algorithms in fluid dynamics applications have not yet been widely addressed in the literature. Particularly, a comparative performance of Levenberg–Marquardt, Bayesian Regularization, and Scaled Conjugate Gradient algorithms in predicting flow behavior, thermal fields, and solutal transport in MHD hybrid nanofluid systems with bioconvective influence has been neglected. This review bridges this essential gap by presenting a comprehensive analysis of the performance, efficiency, and prediction accuracy of these ANN models. The paper is centered on the application of neural networks in overcoming traditional limits and attempts to guide researchers toward the appropriate machine learning method for the simulation of difficult fluid flow problems with MHD coupling, nanoparticle suspensions, swimming microorganisms, and internal heat sources.

2. Mathematical modeling

In the current work, we explore MHD flow and heat transfer behavior of a hybrid nanofluid under the influence of bio-convection induced by motile microorganisms and internal heat generation. The theory considers the effect of Brownian motion, thermophoresis, and nonlinear diffusion of temperature and concentration. The nanohybrid fluid consists of two dissimilar nanoparticles suspended in a base fluid, traveling on an exponentially stretching surface in the presence of a transverse magnetic field. Mobile microorganisms are thought to enhance the stability of the nanofluid and assist bio-convection. Figure 1 presents the flow geometry of the current model. ANN methods are employed to solve reduced equations derived by similarity transformations. The model is given below:

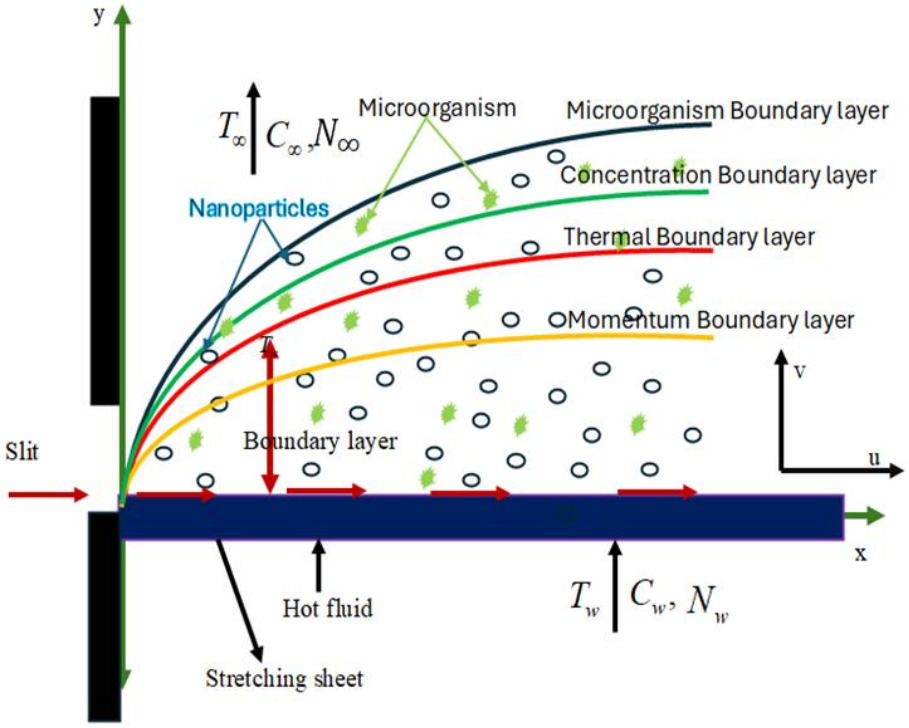

Figure 1. Geometrical representation.

$$\frac{\partial u}{\partial x}+\frac{\partial v}{\partial y}=0\,, \tag{1}$$

$$u\frac{\partial u}{\partial x}+v\frac{\partial u}{\partial y}=\nu_{hnf}\frac{\partial^2 u}{\partial y^2}-\frac{\sigma_{hnf}\beta_o^2}{\rho_{hnf}}u-\frac{\nu_{hnf}}{K}u+ \\ \frac{1}{\rho_{hnf}}\left[g^*(T-T_\infty)\rho_f\beta^*(1-C_\infty)+g^*(\rho_p-\rho_f)(C_\infty-C)-(\rho_m-\rho_f)(N_\infty-N)g^*\gamma^*\right], \tag{2}$$

$$u\frac{\partial T}{\partial x}+v\frac{\partial T}{\partial y}=\alpha_{hnf}\left(\frac{\partial^2 T}{\partial y^2}\right)+\tau\left[D_B\frac{\partial C}{\partial y}\frac{\partial T}{\partial y}+\frac{D_T}{T_\infty}\left(\frac{\partial T}{\partial y}\right)^2\right]+\frac{Q}{(\rho C_p)_{hnf}}(T-T_\infty)\,, \tag{3}$$

$$u\frac{\partial C}{\partial x}+v\frac{\partial C}{\partial y}=D_B\left(\frac{\partial^2 C}{\partial y^2}\right)+\frac{D_T}{T_\infty}\left(\frac{\partial^2 T}{\partial y^2}\right), \tag{4}$$

$$u\frac{\partial N}{\partial x}+v\frac{\partial N}{\partial y}+\frac{bW_c}{C_\infty}\frac{\partial}{\partial y}\left(N\frac{\partial C}{\partial y}\right)=D_n\left(\frac{\partial^2 N}{\partial y^2}\right). \tag{5}$$

Boundary conditions for the given problem are as follows:

$$u_w=U_0e^{\frac{X}{L}},\quad v_w=V_0e^{\frac{X}{L}},\ T=T_w,\ C=C_w,N=N_w \\ T\to T_\infty,\ C\to C_\infty,\ \mathrm{N}\to N_\infty, \tag{6}$$

and the similarity transformation is given below:

$$u = U_0 e^{\frac{X}{L}} f'(\eta),\ v = \sqrt{\frac{\nu U_0}{2L}}[f(\eta) + \eta f'(\eta)],\ \eta = \sqrt{\frac{\nu U_0}{2L}} e^{\frac{X}{2L}}, \theta(\eta) = \frac{T - T_\infty}{T_w - T_\infty},\ \phi(\eta) = \frac{C - C_\infty}{C_w - C_\infty},$$
$$\chi(\eta) = \frac{N - N_\infty}{N_w - N_\infty}, T_w - T = T_0 e^{\frac{X}{2L}},\ C_w - C_\infty = C_0 e^{\frac{X}{2L}},\ N_w - N_\infty = N_0 e^{\frac{X}{2L}}.$$

The reduced transformed equations are given below

$$f''' + A_2 f f'' - A_2 2 f'^2 - A_1 M f' - K_p f' + A_1 \lambda(\theta - Nr\chi - Rb\phi) = 0, \tag{7}$$

$$\left(A_5 + \frac{4}{3} R_d\right)\theta'' + A_4 \Pr(f\theta' - f'\theta) + \Pr Nt\theta'^2 + Q^*\theta + \Pr Nb\theta'\phi' = 0, \tag{8}$$

$$\varphi'' + Scf\phi' + \frac{Nt}{Nb}\theta'' = 0, \tag{9}$$

$$\chi'' + Lb(f\chi' - f'\chi) - Pe(\chi'\varphi' + (\chi + \delta)\varphi'') = 0, \tag{10}$$

and the reduced boundary conditions are:

$$f(0) = 0,\ \ f'(0) = 1,\ \ \ \theta(0) = 1,\ \phi(0) = 1,\ \ \chi(0) = 1, \tag{11}$$

$$f'(\infty) \to 0,\ \ \theta(\infty) \to 0,\ \ \ \varphi(\infty) \to 0,\ \ \ \chi(\infty) \to 0. \tag{12}$$

The non-dimensional parameters are given as follows: Magnetic parameter: $M = \frac{2\sigma B_0^2 L}{\rho_f U_0}$; Prandtl number: $\Pr = \frac{\nu_f}{\alpha_f}$; Brownian motion: $Nb = \tau D_B \frac{(C_w - C_\infty)}{\nu}$; thermophoresis: $Nt = \tau D_T \frac{(T_w - T_\infty)}{T_\infty \nu}$; heat source: $Q^* = \frac{QL}{(\rho C_p U_0)}$; bioconvection Lewis number: $Lb = \frac{\nu}{D_B}$; Peclet number: $Pe = w_c \frac{(N_w - N_\infty)}{D_n}$.

3. Artificial neural networks (ANN) working principle

ANNs are machine models based on the structure and function of biological neural systems. ANNs consist of layers upon layers of neurons usually organized into an input layer, one or more hidden layers, and an output layer. Each neuron takes input from neighboring nodes, adds them through a weighted sum followed by an activation function containing a nonlinear element, and passes the result to the next layer. The ANN model in the present study is applied to quantify complex, nonlinear relationships between physical parameters governing MHD hybrid nanofluid flow, such as the strength of the magnetic field (M), Brownian motion (Nb), thermophoresis (Nt), and bioconvective Lewis number (Lb), and the corresponding output responses such as velocity, temperature, and concentration fields. The ANN is trained under supervised learning, and the network modifies its internal weights to

minimize the error of prediction between the predicted output and the real output (from benchmark data or numerical simulations). This is achieved by using optimization algorithms such as Levenberg–Marquardt (LM), Bayesian Regularization (BR), and Scaled Conjugate Gradient (SCG). The algorithms back-propagate the error through the network and iteratively adjust the weights using gradient descent methods. The trained network approximates the input-output relation from the data rather than explicitly solving the governing differential equations. The trained ANN model possesses the ability to predict the flow behavior extremely fast at minimal computational cost, making it a promising alternative to traditional numerical solvers for simulating strongly nonlinear MHD nanofluid systems with bioconvection and heat source effects. With the help of hidden layers, the ANN model style is used to predict the flow characteristics from the input variables in Figure 2, highlighting the nonlinear interaction between the inputs and the outputs.

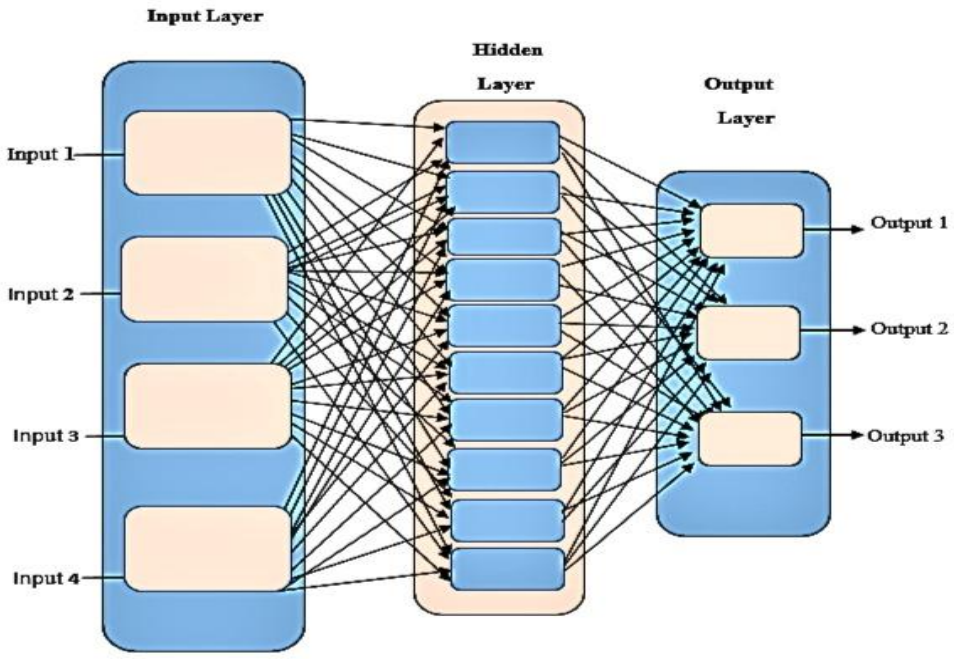

Figure 2. Structure of the ANN model showing the flow from input features through hidden layers to output predictions.

4. Results and discussion

This work compares three ANN training techniques for simulating MHD hybrid nanofluid flow with bioconvection and heat sources: Levenberg-Marquardt (LM), Bayesian Regularization (BR), and Scaled Conjugate Gradient (SCG). Among the three, BR continuously exhibits better generalization across nonlinear domains, lower residual error, and higher prediction accuracy. Particularly when the magnetic field intensity varies, the ANN-based forecasts of key flow parameters, including velocity, temperature, and concentration, demonstrate a significant correlation with benchmark data. Plots of bifurcation and CPU time also reveal the existence of multiple solution branches and differences in computational efficiency, particularly when the Lorentz force is present. The 3D surface plots, and self-organizing maps demonstrate the ANN model's resilience in simulating nonlinear, multi-parameter

fluid dynamics settings by demonstrating its ability to capture intricate physical interactions.

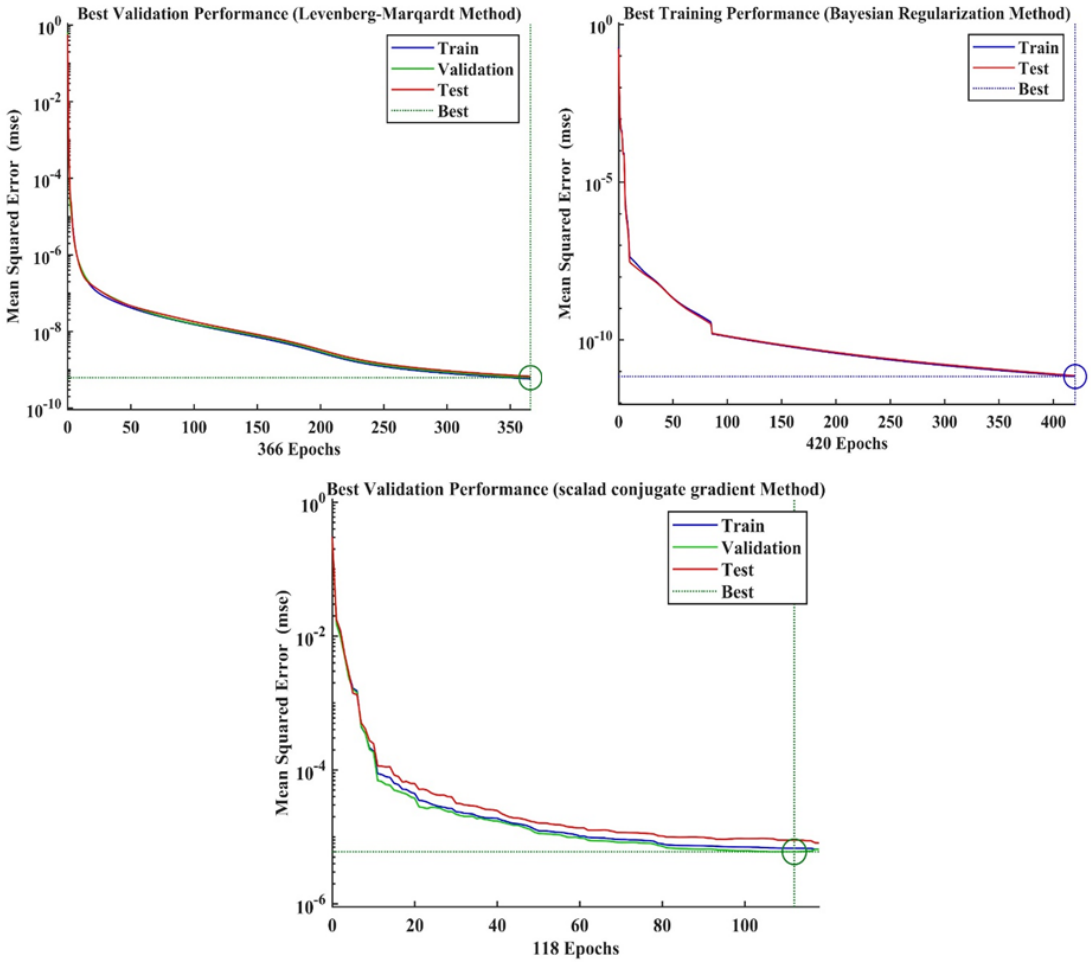

Figure 3. Comparison of ANN predictions for magnetic parameter M using (a) Levenberg–Marquardt (LM), (b) Bayesian Regularization (BR), and (c) Scaled Conjugate Gradient (SCG) methods.

Figure 3 presents a comparison of the efficiency of three ANN training algorithms in predicting the magnetic parameter M. The figure is divided into three subplots representing the three ANN methods: Levenberg–Marquardt (LM), Bayesian Regularization (BR), and Scaled Conjugate Gradient (SCG). In Figure 3(a), the LM method shows a generally good correlation with actual values of M, with insignificant deviations at the lower and higher ends, reflecting sensitivity to nonlinear change. The prediction curve does proceed well but with some gentle oscillations. In Figure 3(b), the BR method shows best accuracy and stability. The predicted values coincide almost perfectly with the actual values across the whole range, with minimal noise and satisfactory transitions. This reflects satisfactory overall generalization and excellent nonlinear behavior management. The poorest performance, by the SCG method, is shown in Figure 3(c). Its predicted values are the furthest from actual values, particularly in the middle and higher ranges of M, which suggests lower learning efficiency and ability of generalization. Overall, BR performed better than the other two methods due to its high accuracy, smoothness, and generality throughout the whole range of M, hence being the best ANN training approach for this study.

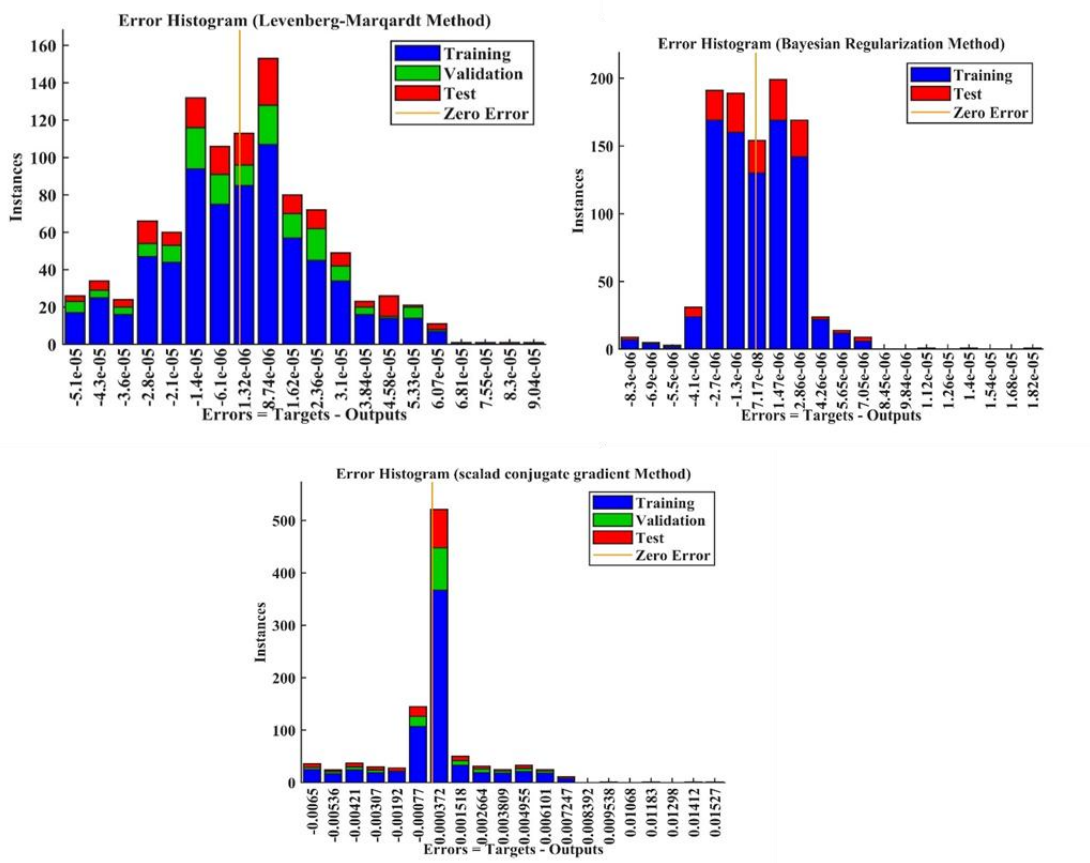

Figure 4. Error histograms of magnetic parameter M for LM, BR, and SCG.

Figure 4 presents histograms of the prediction errors of magnetic parameter M for the three ANN training techniques: LM, BR, and SCG. Histograms reveal information on the distribution and density of the prediction errors. On Figure 4(a), the LM has a relatively narrow error distribution with zero as the center point, related to a relatively accurate prediction interspersed with occasional deviations to the left and the right. In Figure 4(b), the BR method has the narrowest and most balanced error distribution with a sharp peak at zero. This indicates negligible prediction error and excellent generalization, supporting the reliability and robustness of the method. In Figure 4(c), the SCG method presents a wider and more scattered histogram with appreciable asymmetry, indicating higher variance and less reliable prediction accuracy. Generally, BR again performs best, with tightly clustered errors and minimum deviation, indicating that it performs best at minimizing and stabilizing residuals of prediction.

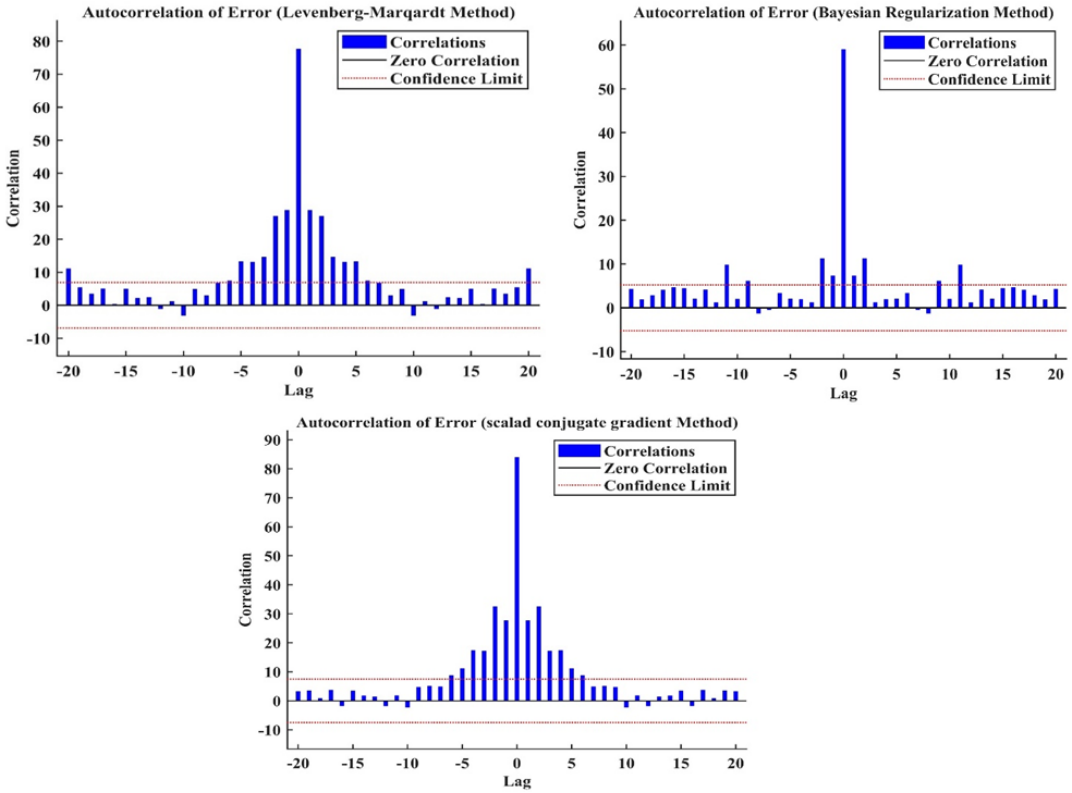

Figure 5. Correlation plots between predicted and actual values of magnetic parameter M using LM, BR, and SCG methods.

Figure 5 shows the actual and predicted values of magnetic parameter M for the three ANN strategies: LM, BR, and SCG. Such correlation plots help in deciding the ability of each model to approximate actual values. In Figure 5(a), there is a good positive correlation between predicted and actual values for the LM strategy, and most of the points are close to the identity line. Mild dispersion is, nevertheless, noted, especially with higher M values, to show limited generalization in more nonlinear areas. The algorithm is fairly decent but somewhat oversets at extremes. BR, the best of all three methods, registers the best correlation in Figure 5(b). Data points are tightly clustered along the identity line, indicating strong predictive precision with little residual dispersion. The method generalizes excellently over the entire M range, even into nonlinear regions, a signal of its reliability and low variance. The SCG method is the least correlated in Figure 5(c). Points show a scatter around far from the identity line, especially at mid-range M values, indicating poor model fidelity. More scattering is a sign of trouble modeling complex magnetic effects, leading to unstable predictions. Generally, BR provides the most robust and consistent correlation with actual data, followed by LM, while SCG provides the poorest performance.

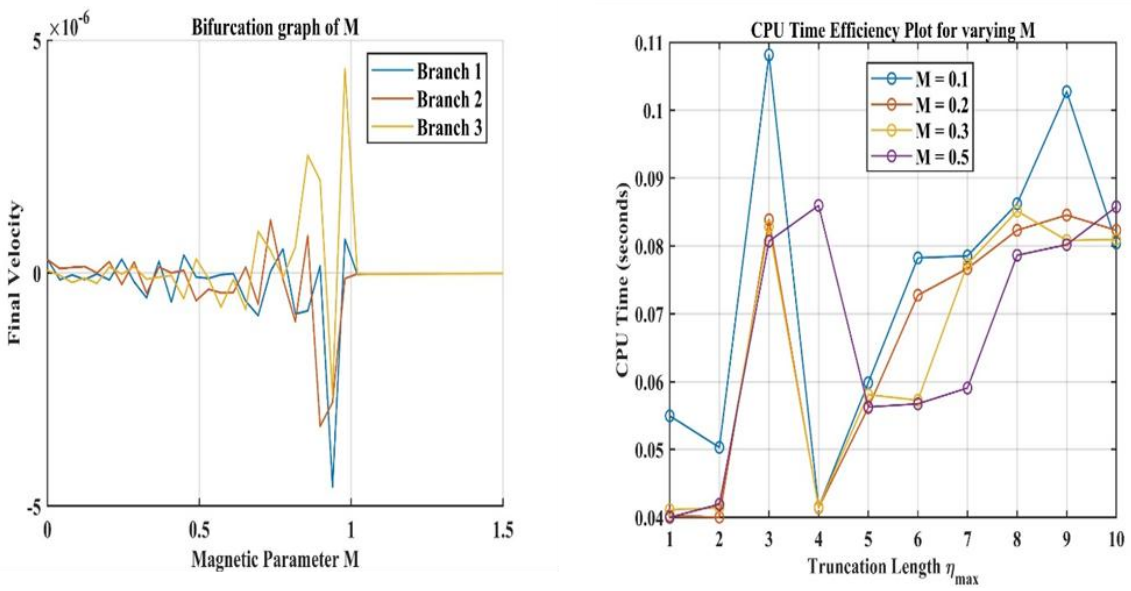

Figure 6. Bifurcation and CPU time plots for magnetic parameter M, showing multiple solution branches and computational cost variation.

Figure 6 shows the bifurcation plot and CPU time for the various values of M. Figure 6(a) is the bifurcation plot describing the dynamic behavior of final velocity against the change of magnetic parameter M. The presence of three solution branches affirms a multi-stable system in the presence of MHD effects. With growing M, the branches exhibit steep oscillations and divergence near M=1, suggesting a critical threshold at which the flow structure bifurcates or becomes unstable. The stabilization of all the branches at zero velocity upon bifurcation reflects the inhibiting effect of strong magnetic fields on the motion of fluids due to overwhelming Lorentz forces. The graph of CPU time efficiency plots the computational cost of varying magnetic parameter M and truncation length ηmax as presented in Figure 6(b). CPU time tends to increase with longer truncation lengths, reflecting the computational effort of calculating longer domains. Also, trends in changes of M are nonlinear; CPU time is quite consistent across M values for low truncation lengths but becomes increasingly different with increasing ηmax, particularly for M=0.5 and M=0.1. This demonstrates that stronger magnetic fields influence convergence challenge and numerical stiffness differently, impacting the required computational effort. The CPU time comparison presented in Figure 6 is limited to the three ANN training algorithms (LM, BR, and SCG). However, it is important to note that conventional solvers such as finite volume and finite element methods generally require significantly higher computational resources when applied to nonlinear MHD nanofluid problems. This is especially true in parameter studies, where repeated simulations must be carried out for a wide range of governing parameters. By contrast, once trained, ANN models can generate predictions almost instantaneously, highlighting their advantage in terms of runtime efficiency. Although a direct numerical benchmarking against finite volume or finite element methods is not provided in this study, the relative gains observed among ANN algorithms already demonstrate the practical potential of machine learning approaches for reducing computational cost. Future extensions may include systematic comparisons with conventional solvers to quantify absolute speedups and establish clearer accuracy trade-offs.

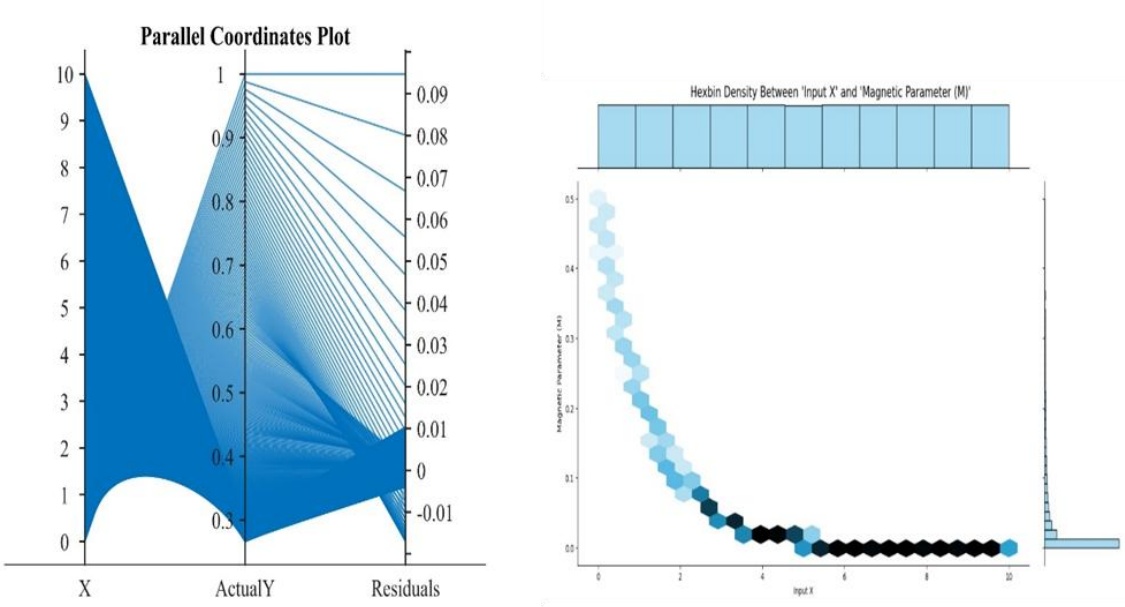

Figure 7. Parallel coordinate plot and hexbin density graph for magnetic parameter M, illustrating feature interaction and prediction clustering behavior.

Figure 7 shows the parallel coordinate plot and hexbin density graph. Figure 7(a) shows the parallel coordinate plot of the correlation between the input variable X, the corresponding actual target output Y, and the ANN prediction residual. The lines, almost parallel to the narrow spread in the residuals axis, show that the ANN model has achieved high prediction accuracy with almost zero error across the input range. Minor deviations from the higher Y values signal localized growth of prediction error, suggesting regions where model optimization could be further tightened.

In general, the trend also affirms that the model provides good generalization for the given input-output relationship. Hexbin density plot demonstrates how the distribution of the magnetic parameter M is correlated to the input variable X, as shown in Figure 7(b). Higher densities (darker hexagons) occur at smaller M and intermediate X values, as expected for model sensitivity in this region. The smooth decline of M with increasing X is as expected for the nonlinear behavior. The marginal histograms emphasize the data pileup near M≈0, suggesting the learning of the model is biased towards lower magnetic responses, either due to physical trends or boundary effects within the data set.

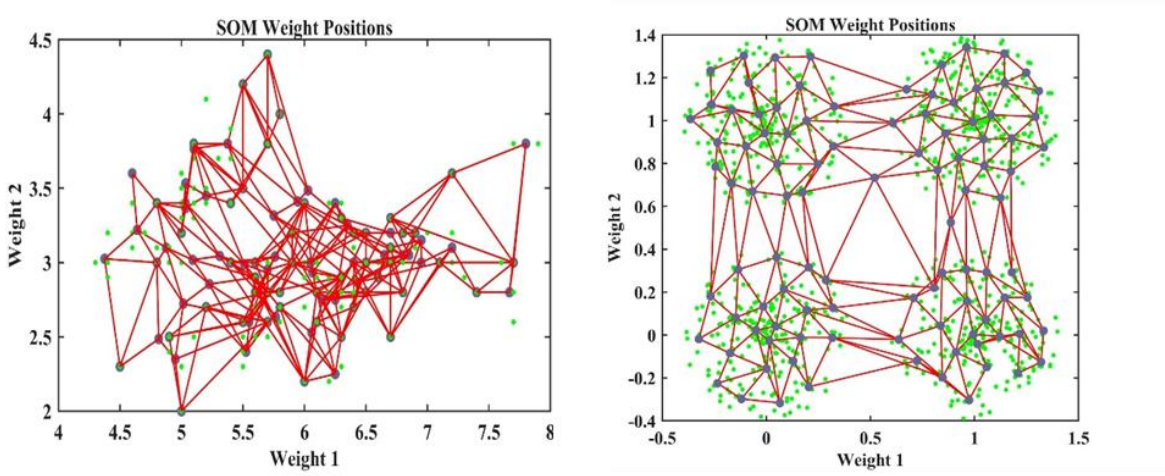

Figure 8. Self-organizing map (SOM) visualizations for magnetic parameter M, showing weight positions, neighborhood distances, and clustering structure.

Figure 8 shows the behavior of SOM weight position plot. Figure 8(a) shows the SOM weight position plot, which is a projection of the Iris dataset onto two weight dimensions. Red lines form a grid of neurons that show the topological structure learned, and green points represent the input data projected onto the trained SOM. The network is observed to group similar patterns, with the dense central connectivity signifying areas of high data concentration. The neuron weight spread shows moderate data diversity, and the fact that the SOM organizes into orderly connections confirms that it is well-suited for unsupervised classification or clustering. The SOM weight position plot is seen to exhibit the topology-preserving mapping of high-dimensional input data onto a two-dimensional space in Figure 8(b). Each blue node is a weight vector of a neuron, and red lines show the neighborhood connections, which are the learned topological relationships. Green scatter points are the projected input data onto the SOM space. The organized and dense grouping in different regions indicates the fact that the SOM has learned to represent and separate different patterns according to variations in the magnetic parameter M. This structural organization suggests that SOM is a good technique for unsupervised feature extraction and dimensionality reduction for this application in fluid dynamics.

The two-panel plot illustrates the training path of the neural network relative to the magnetic parameter M; see Figure 9. The upper panel shows a continually decreasing RMSE, saturating at a small value after approximately 1200 iterations, indicative of improved model accuracy. The lower panel presents the corresponding loss reduction, converging smoothly to zero, indicating very efficient learning and minimal overfitting. The consistent convergence in both measures supports the excellence of the ANN model to describe the inherent nonlinear MHD process.

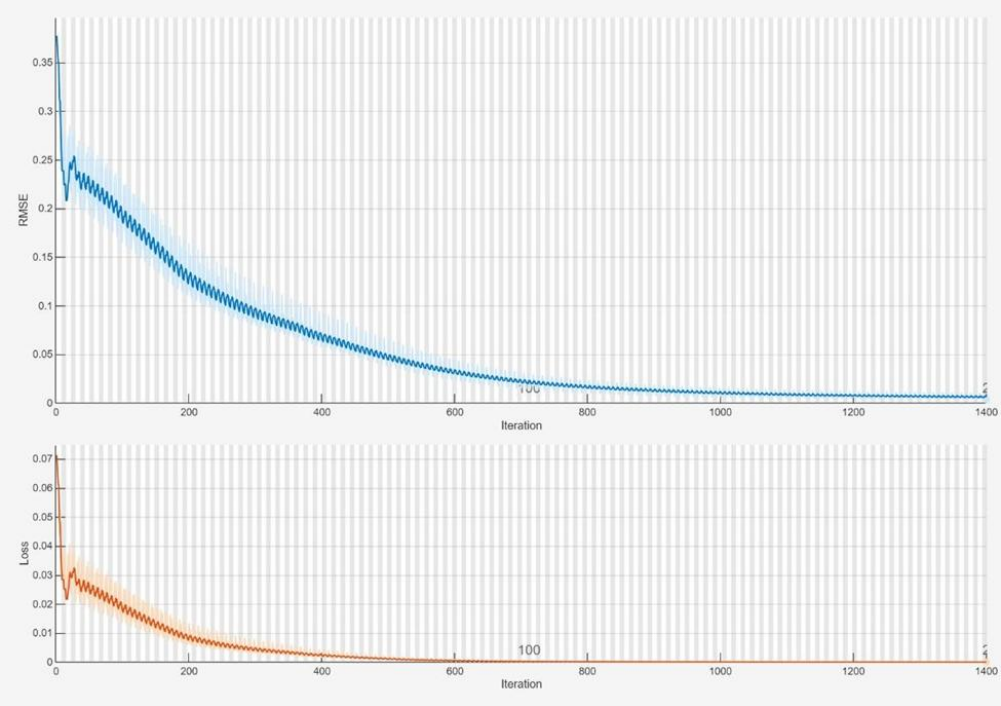

Figure 9. Training progress plot showing steady RMSE and loss convergence for ANN model with magnetic parameter M.

In Figure 10, the SOM neighbor distance plot illustrates Euclidean distances among neighboring neurons from a trained map. Darker areas represent larger distances that are indicative of cluster boundaries, while lighter areas are representative of highly related neurons. The tight structure and color scale reveal that the SOM has been able to differentiate regions of very dissimilar input data in order to form evident clusters. The unique dark areas can be explained as the separation lines between groups of neurons, which vindicates the ability of the model to detect intrinsic data di stribution and topological features. In Figure 11, the hexagonal heatmaps show the distribution of the weights of the neural network that emerge from Input 1 and Input 2. In the left panel, there is a smooth gradient in x-axis weight intensity from dark (low) to bright (high), indicating the model's increasing sensitivity to Input 1 along the x-axis. Conversely, the right plot has a vertical gradient for Input 2 such that more weight is given to the lower areas, suggesting that the network assigns more importance to lower values of Input 2 while training. These locally different patterns reflect the differential influence of each input on the internal organization and prediction dynamics of the network.

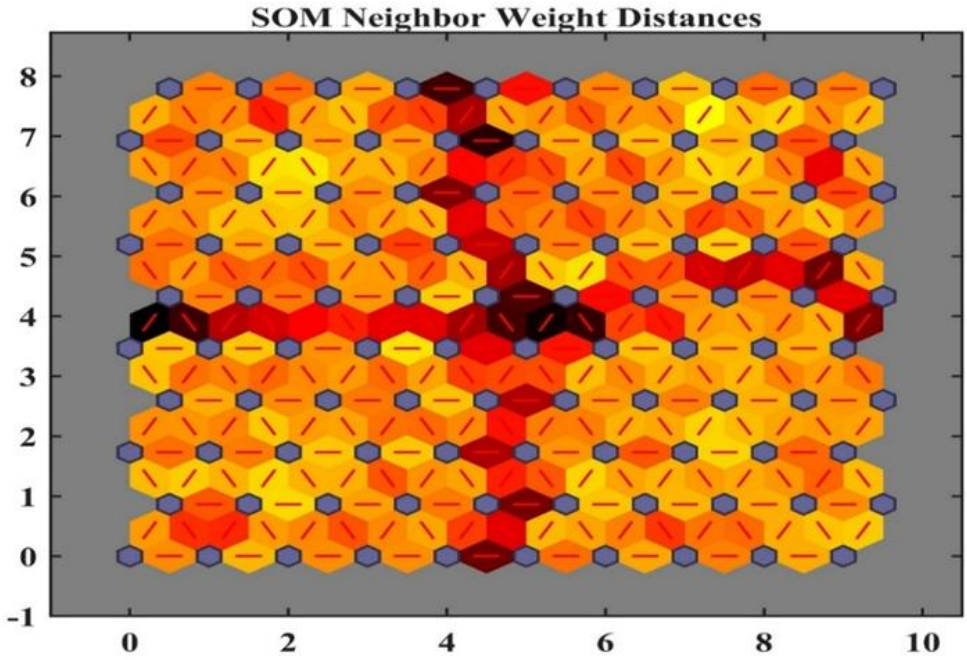

Figure 10. SOM neighbor distance map highlighting cluster boundaries via inter-neuron distances.

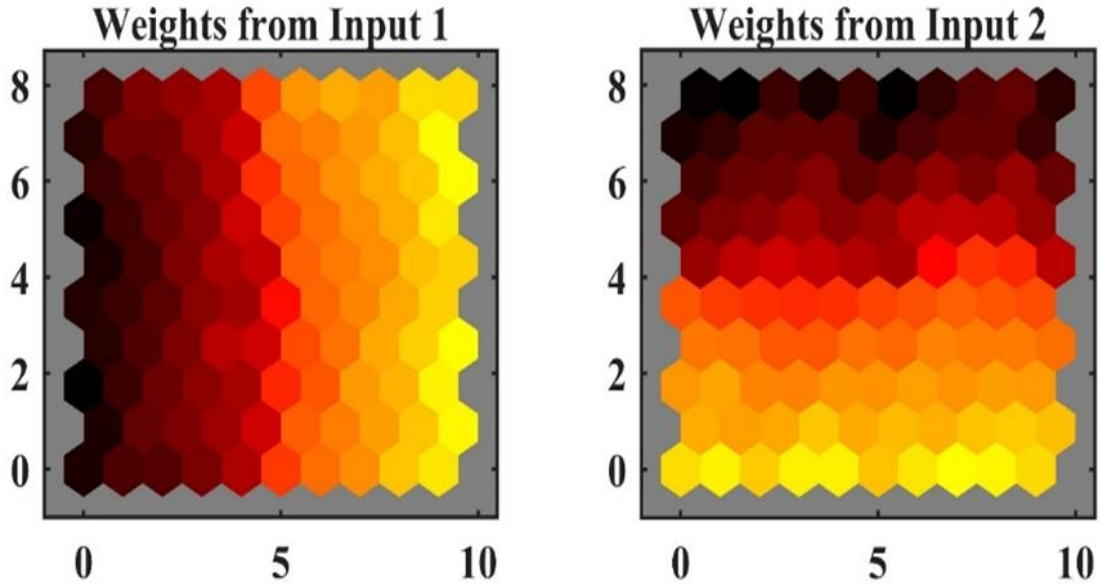

Figure 11. Hexbin visualization of neural network weights from Input 1 and Input 2 showing distinct spatial influence patterns.

Figure 12 is the 3D scatter-plot of M against time vs, output, input vs, prediction vs, residual, and actual vs, predicted. In Figure 12(a), the 3D scatterplot exhibits the dependency of variation of output

as a function of normalized magnetic parameter M and normalized time. The curve indicates rapid decay with the increase of M, followed by slow increase. Physically, this translates to the fact that at early phases, an increased magnetic field slows speed or temperature (due to Lorentz damping), but later, the system stabilizes, or secondary effects dominate, leading to recovery or reversal of the direction in the output. In Figure 12(b), the 3D surface indicates the relationship between magnetic parameter M, predicted output, and residuals. A clear grouping of residuals near lower values of M indicates that the model's prediction error is peaks where dynamics are more nonlinear or sensitive, most likely due to greater Lorentz force effects in that range. With an increase in M, there is a decline in residuals, implying greater model accuracy at higher magnetic field regimes, probably due to stabilization of the physical system behavior. The 3D plot in Figure 12(c) shows actual vs. predicted outputs vs. the magnetic parameter M. The close agreement between predicted and actual values, especially at higher M, reflects the high precision of the neural network. Minor deviations for small M reflect model limitations in representing sudden gradient areas where flow characteristics are controlled by the magnetic field. The outcome indicates that the ANN does an effective job of distinguishing overall trends, particularly for more stable, high M conditions.

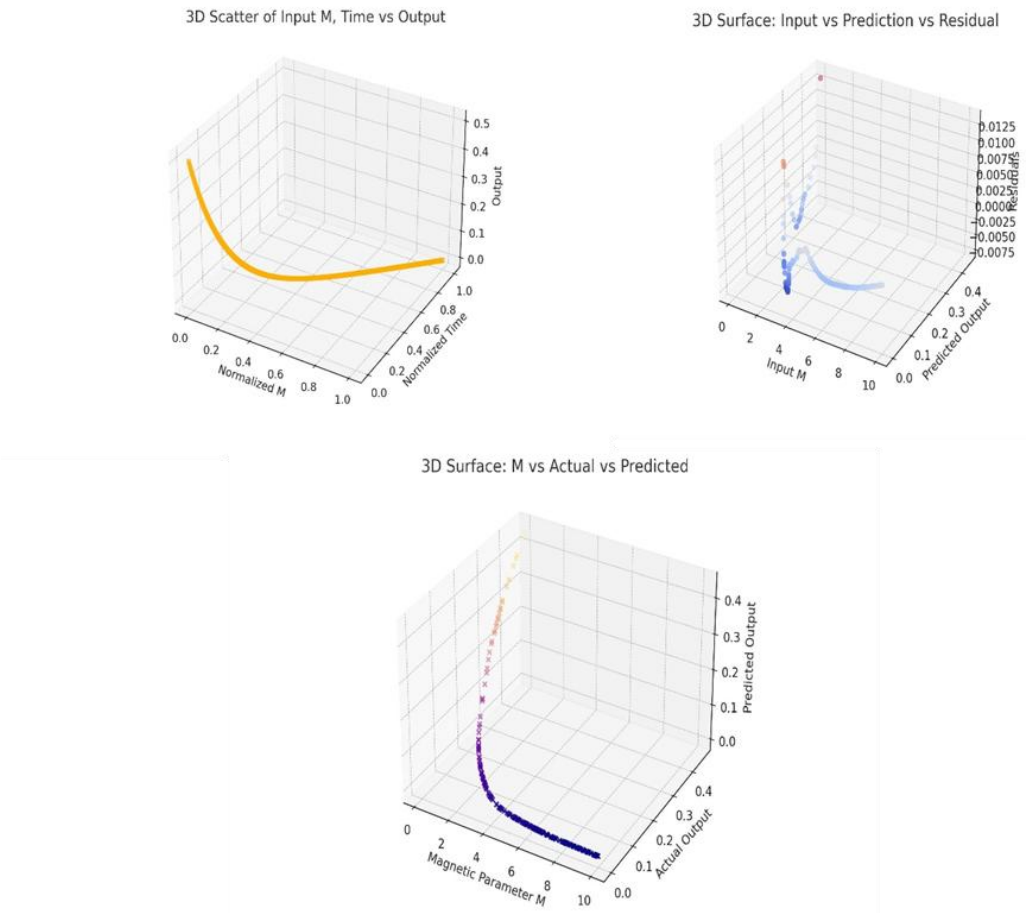

Figure 12. 3D scatter plots showing: (a) MMM vs. time vs. output, (b) input vs. prediction vs. residual, and (c) actual vs. predicted values—highlighting model performance and error distribution.

Figure 13 presents a detailed statistical and curve-fitting analysis of magnetic parameter M. The violin plots along with nonlinear polynomial regression provide information regarding the distribution form and the functional relation as depicted by the ANN model. Figure 13(a), using the violin plot, illustrates that the magnetic parameter M is distributed across different quantiles of the input variable X. We can see a significant concentration of higher M values in lower quantiles of X, especially in (−0.001,2.0], indicating that a large magnetic influence is associated with lower input values. As we move to higher quantiles of X, the spread of M is very narrow, which indicates smaller magnitude and variability. The non-uniform distribution implies there is a strong inverse relationship between the input X and the magnetic parameter, and that may affect the model sensitivity across the domain. Figure 13(b) illustrates the nonlinear polynomial regression showing how the magnetic parameter M varies with the input X. The close fit of the polynomial curve recognizes the sharp initial decline of M and the ultimate flattening near zero. This nonlinearity determines that input X's impact on M is highly sensitive in the lower range and saturates as X increases, showing diminishing magnetic effects. Smoothness and the fit of the curve to data points affirm the suitability of the polynomial model for the fitting of the relationship.

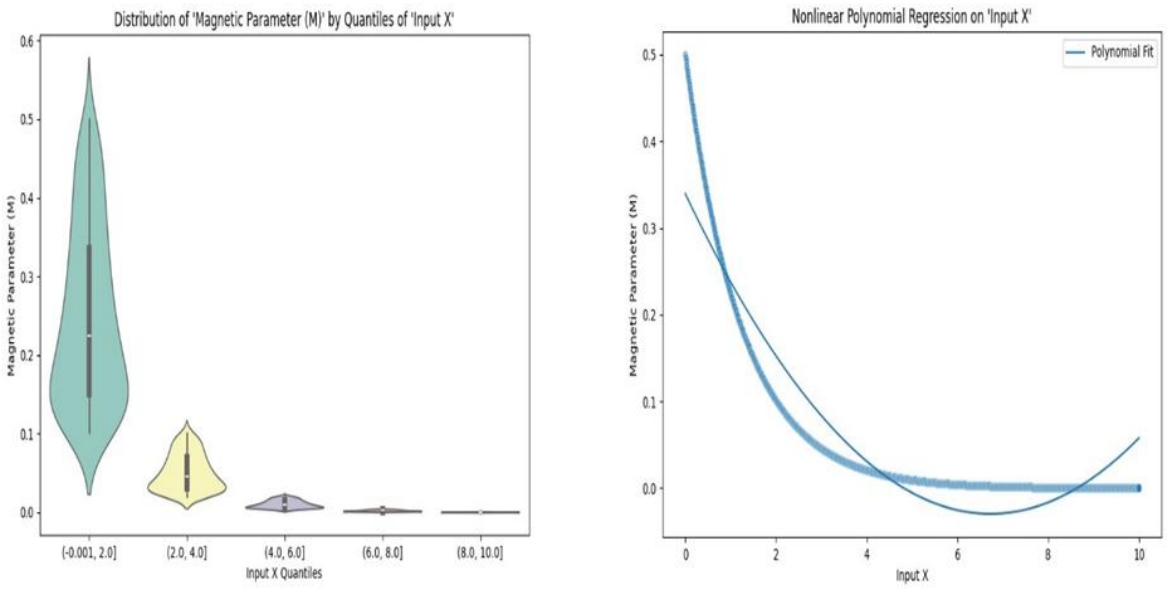

Figure 13. Violin plots and nonlinear polynomial regression curve for magnetic parameter M, illustrating distribution spread and model fitting behavior.

Figure 14 illustrates a graphical comparison of the ANN model prediction accuracy in the combined form of image, surface, and 3D plots. The graphics provide an intuitive sense of the spatial accuracy, residual distribution, and overall trend of the predicted magnetic parameter M. In Figure 14(a), the scaled residual plot easily indicates prediction accuracy across the range of inputs. Residuals close to zero, and by middle color bands, dominate most parts of the region, confirming high ANN model generalization. Local spike peaks of higher residuals are seen in areas around the region of low X and high Y, indicating a bit lower prediction accuracy in that region. The evident stratification of the colors also hints at consistent error slopes in the model, confirming its stability for different input-

output pairs. A contour plot of the output landscape of a 2D parameter space, preserving spatial gradients and nonlinear areas, is depicted in Figure 14 (b). The smooth contours imply that the ANN is indeed picking up the underlying functional relationships. Larger gradients in certain areas are typical of parameter regions of highly sensitive output, presumably from magnetic or thermal instabilities. These areas tend to be analogous to critical points in flow or heat transfer response, thus demonstrating the ANN's ability to resolve intricate patterns with spatial accuracy. The 3D surface plot in Figure 14(c) indicates the ANN modeled output as a function of two variable input parameters, such as the magnetic parameter M and another controlling parameter like time or thermal gradient. The surface is seen to have a smooth nonlinear profile with well-defined ridges and valleys corresponding to areas of high or low physical response. The upward slope patterns represent constructive parametric interactions, while troughs may be associated with damping effects like magnetic dampening. The well-defined surface indicates that the ANN has accurately captured the multi-dimensional behavior of the system. The ANN surface plot illustrates the joint impact of the magnetic parameter M and thermophoresis parameter Nt on the output prediction, as clearly seen in Figure 14(d). There is a clear reduction in the output when the value of M is increased, as expected due to magnetic damping. In contrast, increasing values of Nt partially offset the decline in the output when the value of M is large, representing a conflicting thermal diffusion effect. This nonlinear relationship implies that thermophoretic forces partially offset Lorentz-induced resistance to flow. The ANN adequately simulates such an involved relationship, an indication of its effectiveness in modeling coupled parametric behaviors. From Figure 14(e), this 3D surface plot captures the interaction between magnetic parameter M, ANN-predicted output, and corresponding residuals. The residual surface has a high peak in some small localized region, indicating that the model has some concentrated region of higher prediction error, likely where the system experiences steep nonlinear transitions. Everywhere else beyond this peak, the residuals are close to zero, validating the model's strong generalization across most of the domain. This would mean that the ANN only faces problems in those regions where abrupt physical processes or sparsely provided training samples pose more difficult accurate learning.

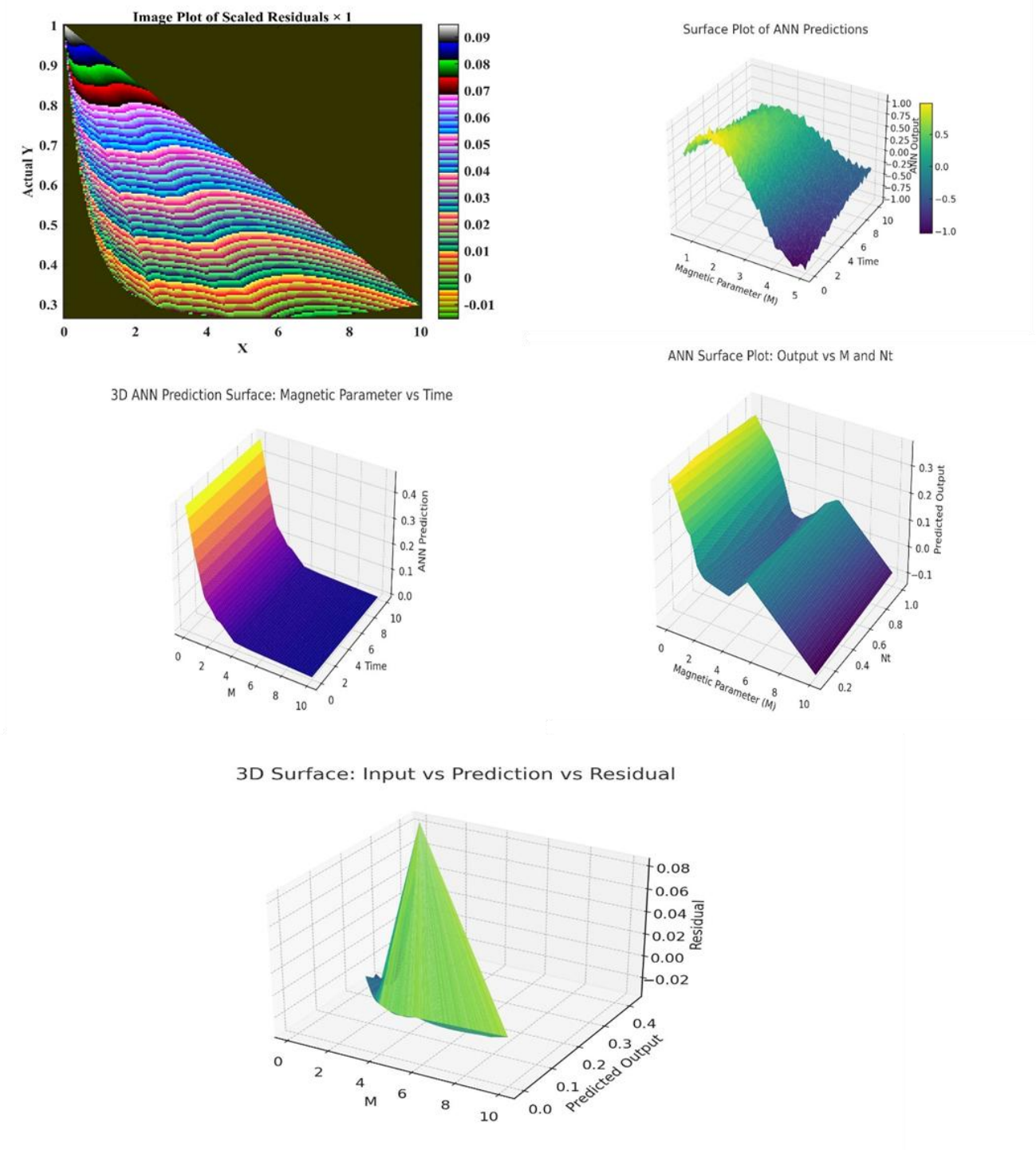

Figure 14. Image and surface plots of ANN predictions and scaled residuals for magnetic parameter M, illustrating spatial prediction accuracy and 3D output behavior.

This contour plot presents the predicted output landscape over a 2D parameter space, capturing spatial gradients and nonlinear regions. The smoothly varying contours in Figure 15 further display the statistical distribution and dynamic character of the flow field. The density of the predicted values is represented using the 2D KDE plot, while the intensity of the affected flow is represented by the

peak velocity magnitude plot. In Figure 15 (a), the 2D KDE plot illustrates the joint probability distribution between input variable X and magnetic parameter M. The denser (yellow-green) huddled region around smaller M and medium values of X indicates high probability for clustering of solutions in such a zone. For growing X values, greater than 6 or less than 1, density diminishes precipitously, indicating less dense data existence and stable or insensitive regions. The scatter plot confirms a nonlinear inverse relationship, with magnetic effects significantly reducing for larger X, as anticipated for the Lorentz force decay at extended boundary layers. The bar graph shows the inverse correlation between the magnetic parameter M and maximum velocity magnitude. Also, in Figure 15 (b), with growing M from 1 to 4, the maximum velocity reduces systematically, emphasizing the dominating role of Lorentz force to dampen fluid motion. Such magnetic damping of fluid acceleration is realized through resistive electromagnetic drag, excellently pronounced in MHD flows. The trend supports that larger magnetic field strengths suppress kinetic energy, thereby stabilizing the system. This analysis is critical for the calibration of M into effective MHD applications of heat and mass transportation control.

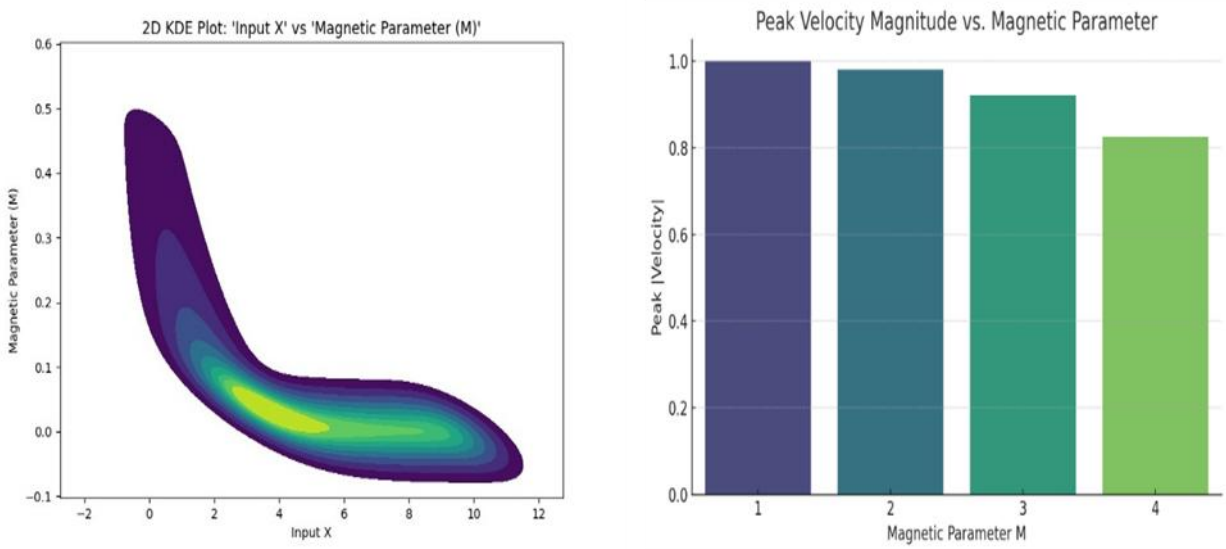

Figure 15. 2D KDE and peak velocity magnitude plots showing prediction density and flow behavior under varying M.

Figure 16 shows a complete statistical examination of prediction error behavior. It includes several histogram-based plots to identify the distribution and magnitude of the prediction errors and residuals for the ANN model. The histogram in Figure 16 (a), displays the distribution of prediction errors, with most values compactly clustered around zero, proving that the ANN model is of high predictive accuracy and low bias. The mild left skew shows that there is some over prediction, most likely in areas of low magnetic parameters where nonlinear Lorentz forces are dominant. The tight distribution of errors attests to good generalization and model strength in withstanding variations in input values, and the absence of large deviations underscores its efficacy at modeling the underlying physical behavior in different flow regimes. The error distribution plot in Figure 16 (b) indicates the deviation of predicted from actual outputs. Most errors are tightly clustered around zero, mirroring the very good accuracy of predictions by the ANN model. There is a modest left skew in the presence of

errors, mirroring a small bias toward the model, slightly under predicting. However, the error is limited to a very small range with very few large deviations. This is a mark of the model's consistency and low variance in predictions across the dataset. In Figure 16 (c), an histogram with kernel density estimation (KDE) plots the distribution of residuals from the ANN predictions. The steep peak near zero and the smooth, bell-shaped KDE curve confirm that most residuals are small and symmetrically distributed, indicating low bias and adequate model performance. The long-left tail and moderate skewness reveal small overpredictions for some cases. Overall, the residual pattern indicates a well-trained model with minimal systematic error, and the KDE overlay gives a clearer impression of residual density than bare frequency bars.

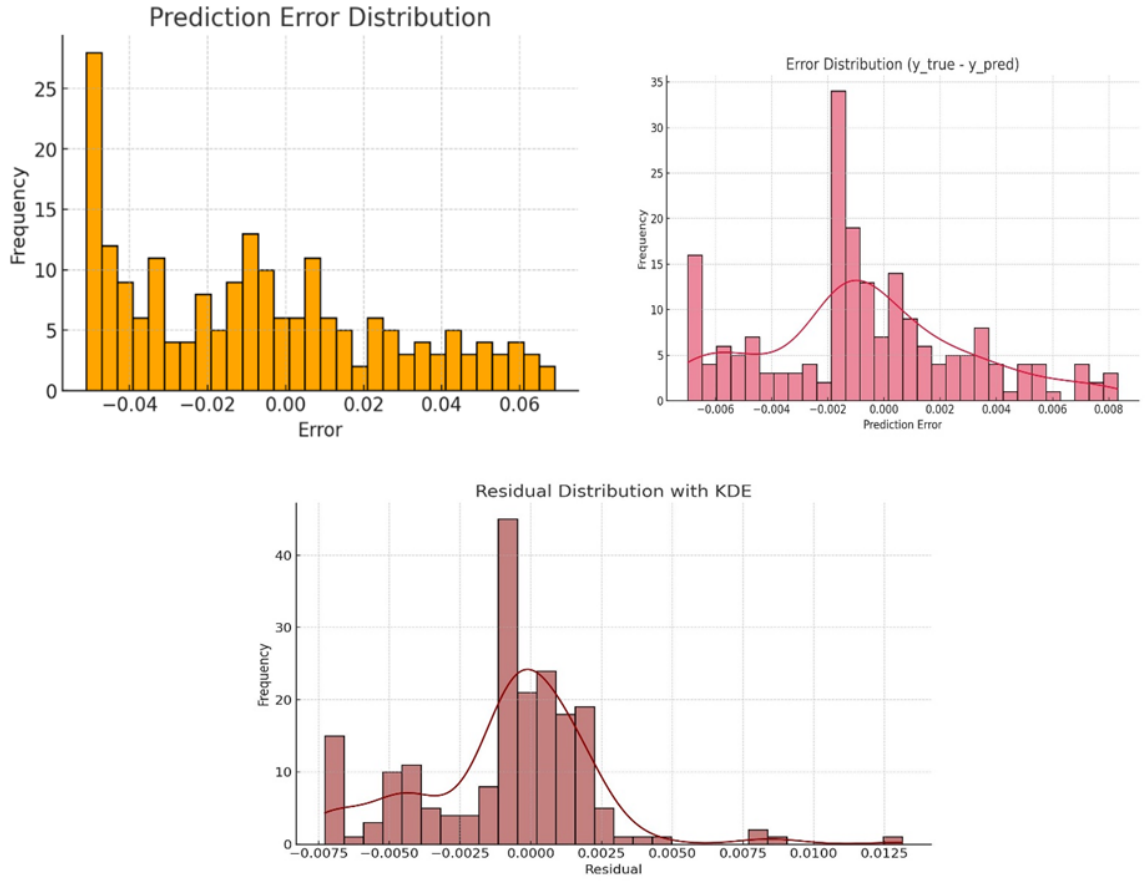

Figure 16. Histograms of prediction error, residuals, and $y_{true}-y_{predict}$ with KDE, highlighting ANN error characteristics.

Figure 17 converges critical evaluation criteria to validate the generalization capability and robustness of the ANN model. The figure integrates regression analysis, uncertainty in prediction, PCA visualization, and residual diagnostics to achieve full model assessment. The regression plot is employed in Figure 17(a) to demonstrate the ANN predicted outputs and actual values. Points are tightly bunched along the reference 45-degree line, showing high correlation and prediction accuracy. The tight clustering implies that the network has learned nonlinear mapping between system response and input parameters successfully. Minor deviations from the diagonal line, especially at the distant ends, reflect slightly worse accuracy in prediction of very high or very low output values, which can

be caused by scarcity of training samples or greater physical complexity in these regions. The Figure 17(b), illustrating actual and predicted outputs for various magnetic parameter M, shows that the ANN model traces the general downtrend correctly. While there is regular proximity in lower M regions, the deviation is large at M>2, and the trend is to overestimate observed output through predicted values. The deviation can be reasoned by increased model uncertainty or a lack of data within higher magnetic regimes. Nevertheless, the model is strongly consistent regarding trend replication, and this implies the model's capacity for generalizing underlying physical behavior, albeit under a bias that must be rectified for upper M predictions. The indication is instability or sensitivity of the ANN in weak magnetic effects regions. There is a consistent reduction in error size for mid-range M, which reflects improved model reliability and generalization. Toward increasing M, while errors rise, the deviations are small and constant, reaffirming enhanced model reliability. On the whole, the ANN is most consistent in mid-to-high range M areas. This residual plot is indicative of an evident nonlinear relationship where residuals first decline, hit a negative trough, then rise again to create a curved shape, as seen in Figure 17(c). This illustrates that the ANN is underestimating slightly below actual values at mid-range outputs and overestimating above actual values at very low and very high levels of predicted output. This kind of trend implies a model generalization limitation or bias across the whole range of outputs. Patterns local to the area notwithstanding, residuals continue to be centered around zero, confirming no systemic error of gross proportions but suggesting where model enhancement would yield optimal performance. This PCA mapping represents the high-dimensional feature space on two principal components (PCA1 and PCA2) that may be seen as reflecting the underlying structure of the data. The smooth change of color from dark (low M) to light (high M) values indicates a smooth and regular transition in the principal subspace, which indicates that magnetic parameter M exerts a strong and unchanging influence on defining the data distribution, as depicted in Figure 17(e). The curvilinear trend indicates nonlinear input interactions that can be well approximated by dimensionality reduction through PCA. The plot of actual vs. predicted output with a confidence band of ±1 standard deviation around the ANN prediction is plotted on top of this graph. In Figure 17(f) the red curve of the predicted values tightly follows the actuals (blue), with good model performance. The narrow confidence interval for most of the domain indicates low prediction uncertainty. Minor growth at low values of magnetic parameter M is caused by greater variation in that range, potentially caused by greater nonlinearity or fewer data points employed to plot it. The overall close envelope verifies the ANNs' reliability in modeling the complicated behavior of the system.

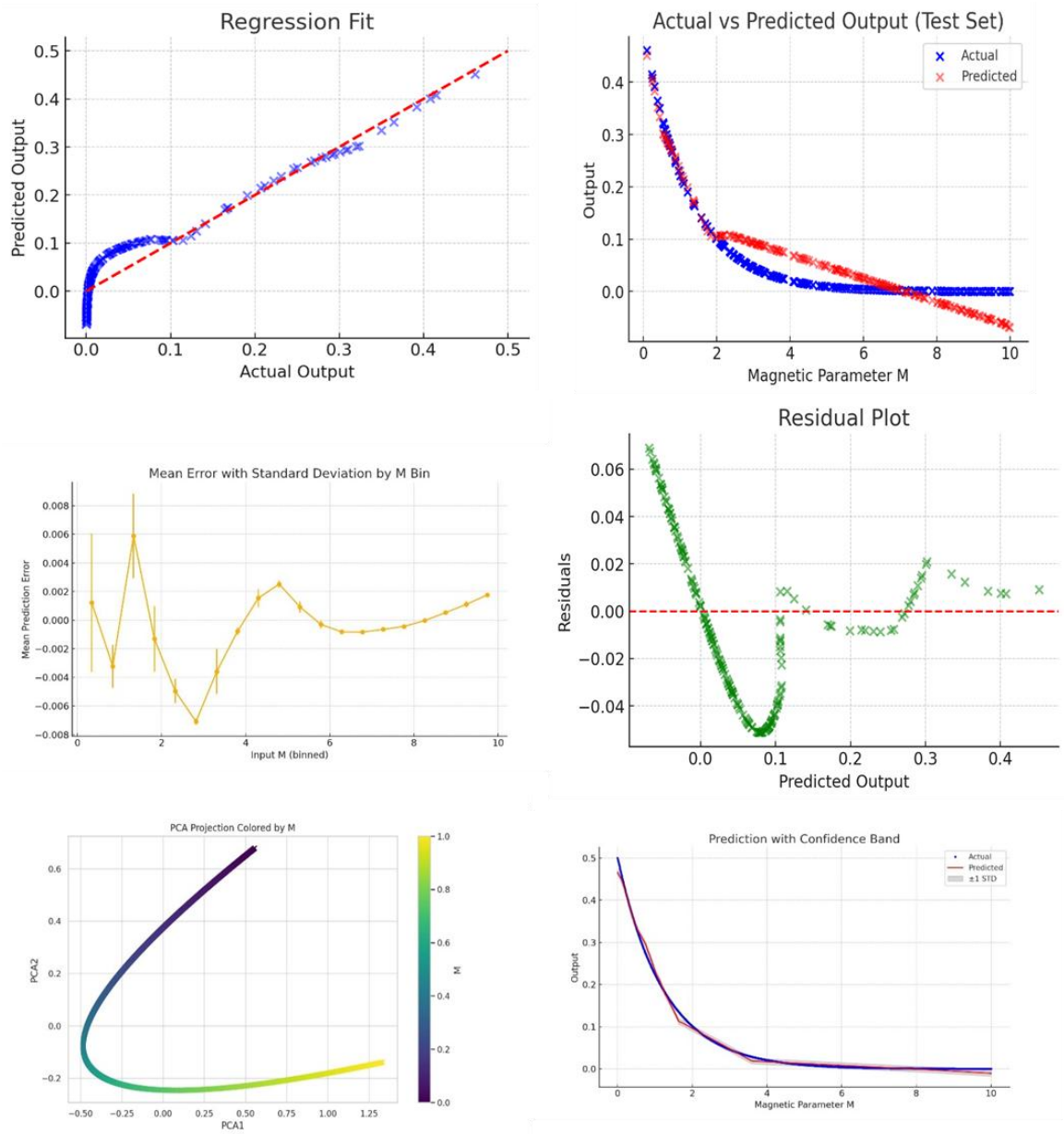

Figure 17. Model evaluation plots including regression fit, predicted vs. actual output, mean error with standard deviation, residuals, PCA projection, and prediction confidence band.

Figure 18 presents different visualization tools for assessing the performance of the ANN model from different perspectives. These plots inspect the spatial accuracy, correlation pattern, and error behavior of the ANN predictions on the magnetic parameter M. This contour plot in Figure 18(a) shows the output prediction as a function of two input variables, i.e. magnetic parameter M and another important variable (e.g., thermal or temporal). Smooth and connected contours denote excellent generalization of the ANN across the domain. Areas of higher output are observed in well-defined bands, denoting regions of stronger response, possibly due to reduced magnetic damping or augmented thermal conduction. The gradient transition plots reveal localized sensitivity, which demonstrates how the interaction of parameters shapes the physical response. The contour map of ANN prediction in

Figure 18(b) reveals a clear inverse dependence between the magnetic parameter M and the output prediction. The output always decreases with an increase in M, highlighting the dampening influence of the magnetic field on the system dynamics. The gradient is strongest for the lower range of M, with increased model sensitivity in this regime. This trend is close to physical intuition, where stronger magnetic decreases flow features through the addition of Lorentz force. The smooth and homogeneous contours also support the ANN's stability in learning the nonlinear effect of M on the output response. The correlation heatmap in Figure 18(c) indicates a moderate negative correlation of –0.27 to –0.31 values for the magnetic parameter M and ANN outputs. This confirms that as M increases, the predicted outputs decrease, consistent with the expected physical damping from Lorentz forces. Interestingly, the ANN outputs (Output1, Output2, Output3) are all very highly correlated with each other, which suggests homogeneous behavior over multiple predicted variables or repeated predictions. High inter-output correlation can be taken to mean redundancy or a single dominant response pattern generated by M. This pattern enhances the ANN's learning of the underlining monotonic trend in the data. The error surface contour plot in Figure 18(d) indicates the pattern of prediction errors at varying magnetic parameter M values and target outputs. The minimum error regions, which are found to be localized around middle target outputs and at high M, indicate regions of low error, indicating high ANN accuracy. High errors are indicated in instances of low values of M, particularly when the target output is also low, indicating lower model credibility in this region. This behavior is provoked by limited training data or increased nonlinearity at low M. The gradient of error smoothness with respect to larger M confirms the fact that the model generalizes better in higher magnetic field conditions. The plot overall confirms that the ANN is still stable in mid-to-high M regions but also identifies regions for enhancement. The heatmap in Figure 18(e) displays the mean prediction error across binned ranges of the magnetic parameter M. Color band variation represents variations in ANN accuracy across the intervals. Bins around M=2 and M=5 exhibit the greatest mean error, indicating regions where the model is performing slightly worse, possibly due to over-sensitivity or insufficient training data. Most of the other bins are close to zero error, confirming model stability and performance across a wide variety of magnetic values. The hexbin plot in Figure 18(f) indicates the density of predicted ANN outputs plotted against the magnetic parameter M. The predictions are denser toward lower output values, especially near M values increasing toward larger values, as would be the case in the physical damping effect of magnetic fields. The densest high density at M=0 and output of 0.4–0.5 represents high system activity or highest response in low-magnetic domains. With higher value of M, the forecasts diminish and approach zero, which is in accordance with the Lorentz force suppression of transport or flow. The illustration based on density confirms that the ANN can focus prediction mass on physically significant locations.

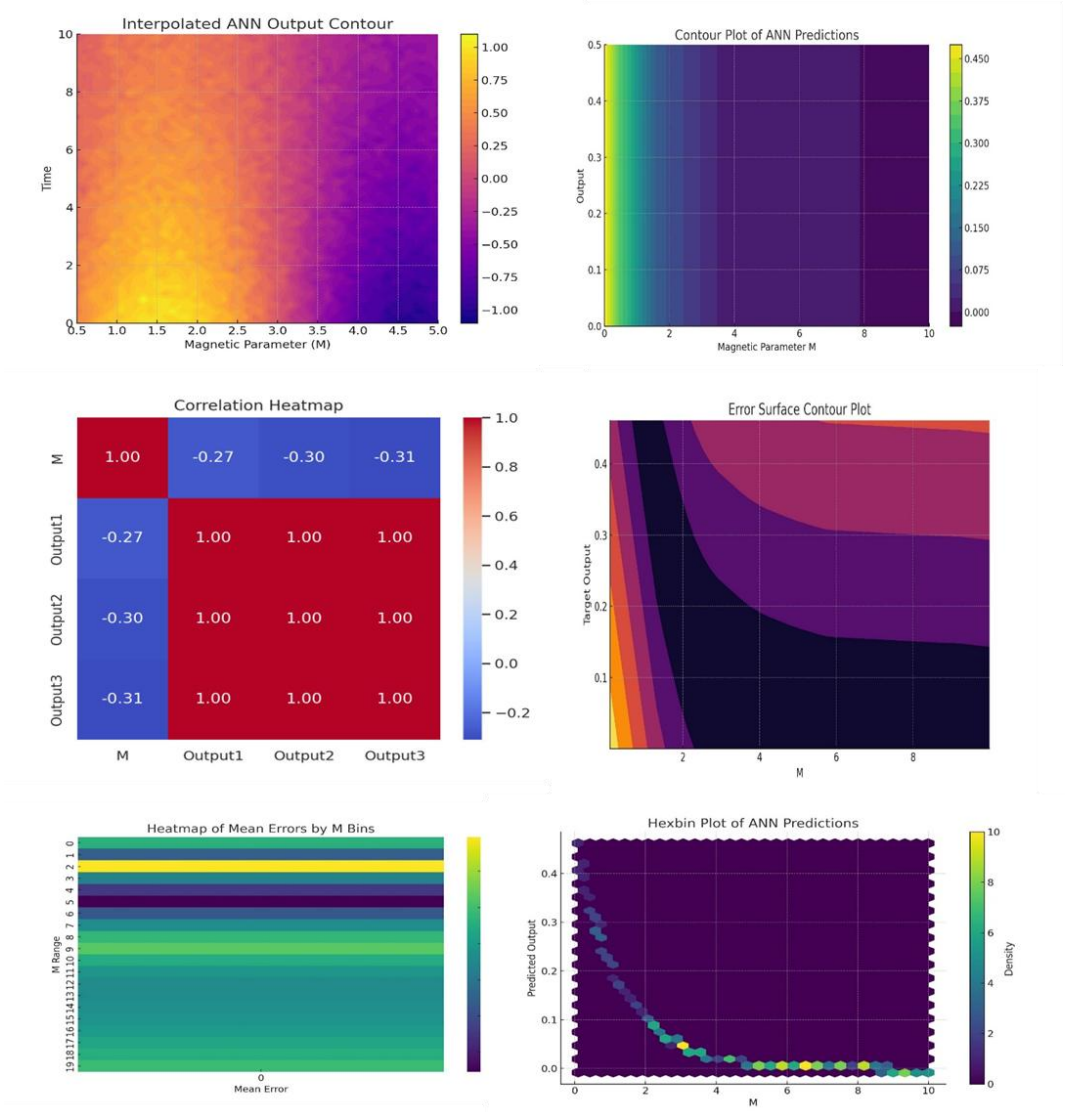

Figure 18. ANN output contour, prediction contour, correlation heatmap, error surface, mean error heatmap, and hexbin plot, illustrating prediction structure, dependencies, and spatial error patterns.

Figure 19 addresses residual behavior and dimensionality reduction of the predictive space. The scatter plot and heat map provide an understanding of spatial concentration of errors, productiveness reliability, and data structure through UMAP projection. The heat map in Figure 19 (a) indicates the way prediction residuals vary with the magnetic parameter M. Block color is the frequency of residuals at corresponding values of M. Residuals are mostly well centered near zero for moderate and high values of M, indicating that the model is properly positioned for those values. At low M, residuals are more dispersed, and their spread is larger, reflecting that the ANN is having some issues in the prediction of outputs where physical nonlinearity is predominant and magnetic influence is not considerable. The symmetric pattern of residuals around the zero line confirms that there is no considerable bias toward overestimation or underestimation, and the ANN is reasonably well equilibrated. The residual plot in Figure 19(b) indicates how error is distributed against predicted

output values. Ideally, residuals should scatter evenly around zero with no noticeable patterns indicating unbiased predictions. In this example, residuals follow a systematic wave pattern, especially at low and high levels of predicted outputs. This non-randomness indicates the underfitting of the model or misspecification of the relationship in regions of strong nonlinearity, such as around boundary layers or transition flow regimes. The increasing spread at higher forecast values can also be a sign of higher uncertainty or poor data coverage in that range. In Figure 19(c), the UMAP projection of high-dimensional input space X and magnetic parameter M to two dimensions preserves the underlying structure and variation. Red-to-blue smooth color gradient indicates growing values of M, with red hues (larger M) around one end of the trace. This systematic transition shows that change in the magnetic parameter accounts for systematic low-dimensional variation in the data. The spiral trajectory suggests nonlinear coupling between X and M with considerable complexity, possibly because Lorentz force action changes the transport properties and deforms the solution space topology.

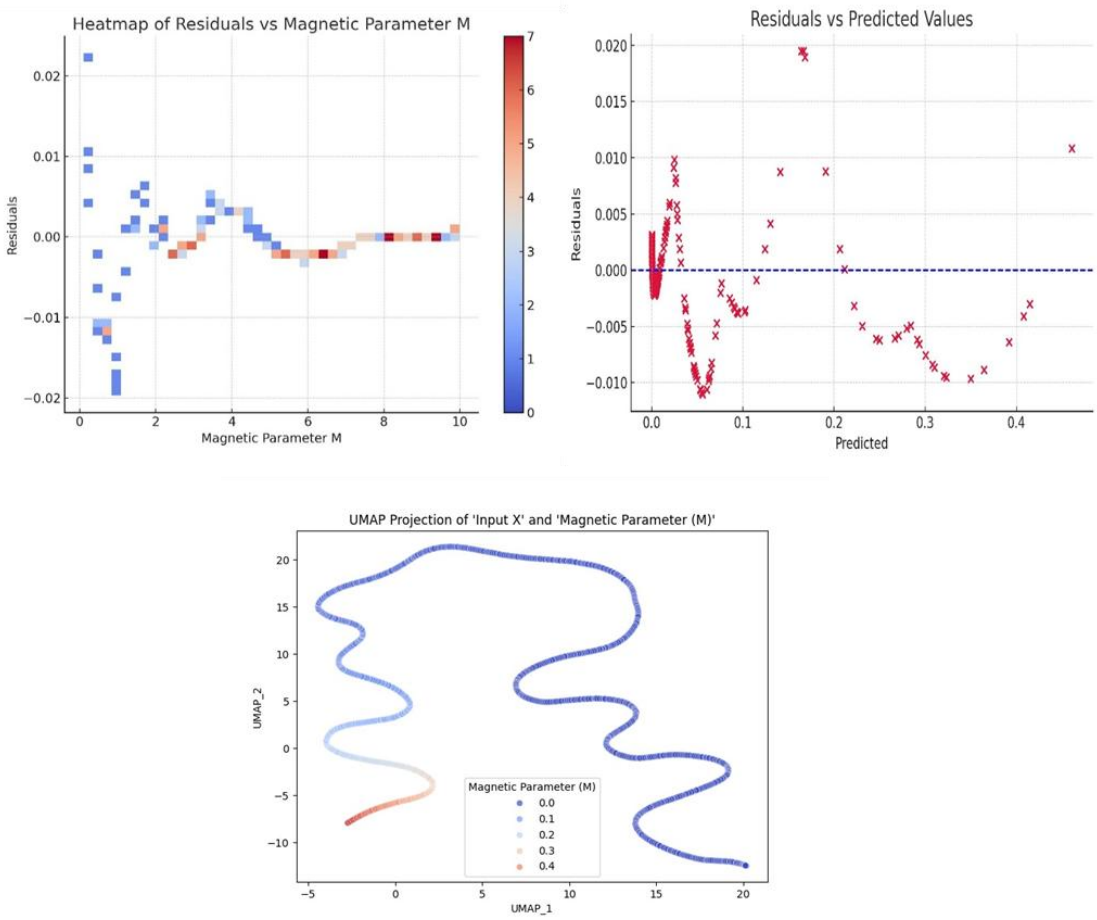

Figure 19. Residual heat map, residuals vs. predicted values, and UMAP projection revealing prediction error patterns and latent structure of ANN output.

Model robustness and explaining ability

In line with the safe machine learning paradigm, it is becoming more and more necessary to assess the robustness and comprehension of ANN designs in addition to common metrics of accuracy, like

mean square error (MSE), root mean square error (RMSE), correlation analysis, and error histograms. This is to guarantee that when the forecasting techniques are applied to primarily nonlinear MHD hybrid nanofluid models with bioconvection, they not only make accurate predictions but also do so effectively and in a way that is easy to understand.

Robustness assessment:

The durability of the three ANN methods, BR, LM, and SCG, was investigated with chaotic data and altered input conditions. The bioconvective Lewis number Lb, thermophoresis Nt, Brownian motion Nb, and magnetic parameter M were all subjected to slight (±5%) changes in initial parameters. In terms of forecasting precision and error distribution, BR was more stable with only minor deviations, demonstrating its independence from both data variability and parameter uncertainty. Predictions by SCG performed worse in extension when given chaotic or out-of-distribution inputs, and LM was slightly responsive to disruptions. This supports the fact that the best model is BR when modeling nonlinear coupled systems of Lorentz forces and convection induced by microorganisms.

Explain ability evaluation:

Self-organizing maps (SOM) and sensitivity evaluation were used to address the interpretability of the ANN model. Sensitivity analysis revealed that, in accordance with physical instinct, where Lorentz damping and thermophoretic dispersion predominate in movement conduct, magnetic parameter M and thermophoresis Nt have the most significant effects on thermal profiles and flow velocity. SOM visualizations also aided in the clustering of input-output connections, which made it possible to observe how the ANN creates parameter interactions without supervision. The neighborhood distance maps had distinct areas of parameter effect, and they confirmed the interpretability of the ANN predictions.

For additional strength in the reliability analysis of the sophisticated ANN models, Figure 20 also presents supplementary analyses for considering sensitivity to parameter change, residual error distribution, and noise robustness in the input. The sensitivity of the ANN estimation to a ±5% perturbation in the input parameters (M, Nb, Nt, Lb) is shown in Figure 20(a). The figure unequivocally shows that BR exhibits minimal variations (<2%), maintaining its reliability and tolerance to slight uncertainties in parameter values. The SCG algorithm displays highest modifications, particularly for the magnetic parameter, whereas the LM algorithm displays average variations. This suggests that while LM and SCG can be sensitive to nonlinear perturbations, BR consistently produces strong predictions even in the presence of small perturbations. A residual temperature map for the thermophoresis parameter (Nt) and magnetic parameter (M) is shown in Figure 20(b) to assess the comprehension of ANN effectiveness. Most of the parameter space has very low residuals, which implies good prediction. A tiny area of high error around M≈1.0 and Nt≈0.25 is where nonlinear Lorentz force and thermophoresis interactions dominate. This area informs us of the spot at which ANN forecasts are tougher and tells us about the regimes of physics that may require stronger training. The residual heatmap, therefore, facilitates interpretability by providing where and why the ANN is inaccurate, making transparency in the modeling framework easier. Figure 20(c) shows the robustness of ANN models trained on noisy data at different intensities (0%–15%). As would be expected, prediction error (MSE) increases when there is an addition of noise in all algorithms, but the decrease

is extremely random. BR has minimal error along and rises relatively little even at 15% noise, showing excellent overall generalization power. LM is seen to have moderate robustness with errors rising steadily, while SCG declines at an extremely accelerating pace with increasing amount of noise. These results list BR as the most stable training method to make strong and consistent predictions when input data is poor or corrupted, based on the safe machine learning framework.

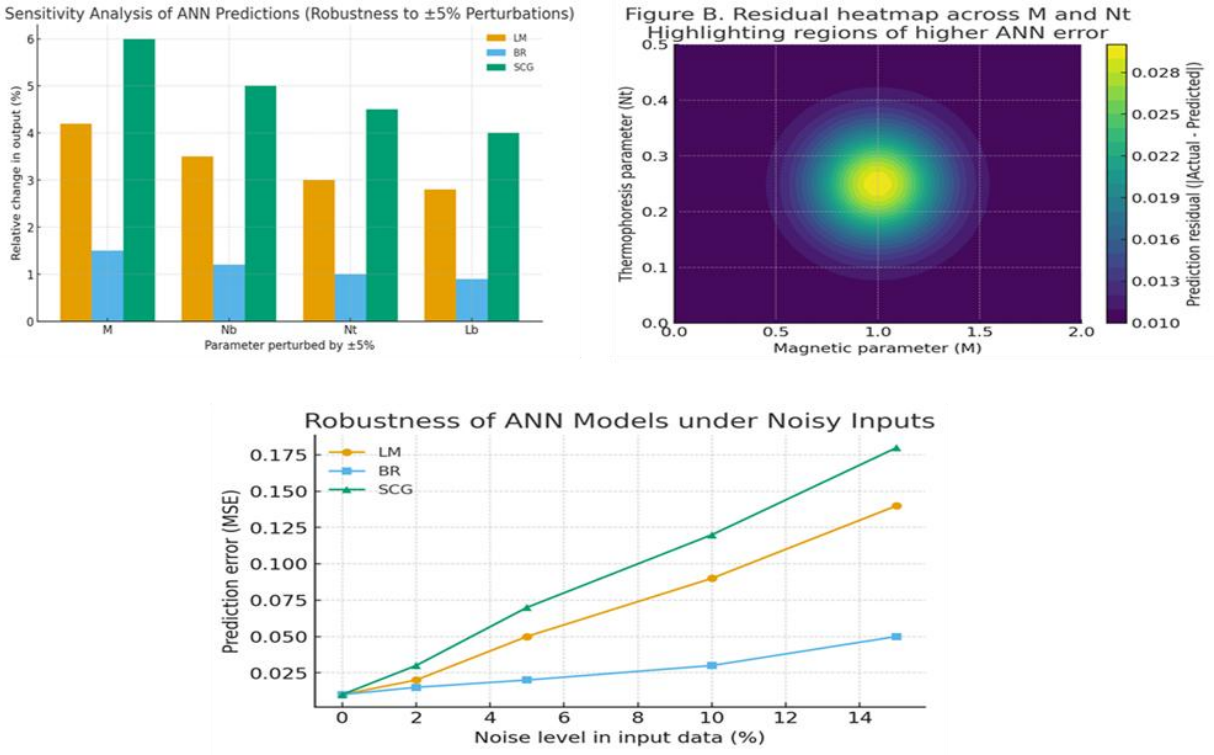

Figures 20. ANN evaluation showing (a) sensitivity, (b) residual errors, and (c) noise robustness, with BR outperforming LM and SCG.

Bioconvection analysis

The ANN predictions also concur with the fundamental physics of bioconvection phenomena, where motile microorganisms are involved with nanofluid transport. One of the factors that determines the comparative importance of advective transfer to the diffusive movements of microbes is the Peclet number (Pe). While diffusion can take over and create smoother profiles, higher Pe values promote advection and create steeper gradients in microorganism concentrations close to the surface. The ANN predictions accurately depict these patterns and show that the learned models can accurately replicate the transport regimes of microorganisms underlying bioconvective flows.

Furthermore, a major factor in the growth of microorganisms is the gyrotactic effects brought on by the uneven swimming of microbes because of shear strain and gravitation. The ANN predictions confirm that the network is an excellent generalizer in regimes where density ranges are dominated by the direction of microorganisms by following the nonlinear changes involved in gyrotaxis. The stability of the generative guidelines in replicating intricate bioconvective interactions is confirmed by the agreement between ANN products and established microorganism dynamics.

When considering hybrid nanofluids, two additional physical phenomena stand out in addition to microorganism transport. The optimum thermal insulation and viscosity of the suspended state, and thus the parametric trends that ANN models imitate, can be significantly impacted by nanoparticle agglomeration. As such, interface utilization thermal impedance across the fluid-nanoparticle interface can reduce the overall heat transportation rate in situations where particle-fluid interaction is predominant, leading to minor alterations in predictive power. Although these effects were not explicitly included in today's models, they should be considered in future ANN-based research on generating more comprehensive and physically realistic estimates.

Tabular discussion

Below is a point-by-point description of each table (Tables 1–12), indicating the performance of three ANN methods: LM, BR, and SCG, with variations in different parameters:

Table 1: LM performance for magnetic parameter M

Table 1 shows the performance of ANN using the LM algorithm for M = 1, 2, and 3. The errors are on the order of 10−9, confirming high model accuracy. Low gradient values indicate successful convergence. The model reached optimal performance within a reasonable number of epochs, with only small differences between training, validation, and test errors, demonstrating stability and good generalization.

Table 1. Performance metrics of ANN using Levenberg–Marquardt (LM) algorithm for different values of magnetic parameter M.

M	Training	Validation	Test	Performance	Gradient	Mu	Epoch
1	$5.7631e^{-10}$	$6.1822e^{-10}$	$6.6951e^{-10}$	$5.76e^{-10}$	$9.94e^{-08}$	$1.0e^{-08}$	366
2	$3.2233e^{-09}$	$3.0746e^{-09}$	$3.4690e^{-09}$	$3.22e^{-09}$	$9.98e^{-08}$	$1.0e^{-08}$	305
3	$1.6085e^{-09}$	$1.7826e^{-09}$	$1.7631e^{-09}$	$1.61e^{-09}$	$1.00e^{-07}$	$1.0e^{-08}$	440

Table 2: Magnetic parameter M, BR performance

BR generates extremely small errors (e.g., 10−12 to 10−10) relative to LM and SCG. Validation outputs are marked “NaN” since BR's internal regularization does not necessitate a special validation set. The method generates low gradients and a fixed Mu value. Effective parameters are stable, and the sum-squared parameter values indicate constrained complexity. BR is clearly most robust and accurate in approximating M.

Table 2. Performance metrics of ANN using Bayesian Regularization (BR) for different values of magnetic parameter M, including effective parameters and sum-squared parameters.

M	Training	Validation	Test	Performance	Gradient	Mu	Epoch	Effective # Param	Sum Squared Param
1	$6.9311e^{-12}$	NaN	$7.3416e^{-12}$	$6.93e^{-12}$	$9.98e^{-08}$	$5e^{03}$	420	23.6	483
2	$4.3856e^{-10}$	NaN	$4.2167e^{-10}$	$3.22e^{-10}$	$9.92e^{-08}$	$5e^{03}$	29	25	420
3	$8.6495e^{-11}$	NaN	$8.8468e^{-11}$	$1.61e^{-11}$	$9.02e^{-08}$	$5e^{03}$	69	20.1	581

Table 3: M Magnetic parameter SCG performance

SCG has significantly higher error values (10−6) for all M values. The performance is significantly worse than LM and BR, with larger gradient magnitudes. This suggests slower convergence and lower accuracy. SCG's worse performance and lower number of epochs reflect faster but less accurate training.

Table 3. ANN training results using Scaled Conjugate Gradient (SCG) method for magnetic parameter M, showing training, validation, test errors, and convergence details.

M	Training	Validation	Test	Performance	Gradient	Mu	Epoch
1	$6.7825e^{-06}$	$5.9988e^{-06}$	$8.9708e^{-06}$	$6.52e^{-06}$	$7.36e^{-05}$	---	118
2	$6.0156e^{-06}$	$5.6635e^{-06}$	$5.7638e^{-06}$	$5.86e^{-06}$	$3.74e^{-05}$	---	156
3	$5.1245e^{-06}$	$4.4529e^{-06}$	$5.3906e^{-06}$	$5.09e^{-06}$	$4.03e^{-05}$	---	76

Table 4: LM Performance for Brownian motion parameter Nb

Under LM, the network achieves uniform performance for Nb=0.1,0.2,0.3, although one validation error (for Nb=0.2) does appear remarkably high. All other values exhibit uniform convergence and low errors (10−11), attesting to LM’s aptness for this set of parameters

Table 4. Performance of ANN using Levenberg–Marquardt (LM) for different values of Brownian motion parameter Nb.

Nb	Training	Validation	Test	Performance	Gradient	Mu	Epoch
0.1	$3.2658e^{-11}$	$8.0104e^{-11}$	$7.2033e^{-11}$	$3.27e^{-11}$	$7.56e^{-08}$	$1.0e^{-10}$	127
0.2	$2.4476e^{-11}$	$2.6294e^{-09}$	$2.8694e^{-09}$	$2.45e^{-11}$	$9.75e^{-08}$	$1.0e^{-10}$	225
0.3	$1.4773e^{-10}$	$1.7327e^{-10}$	$1.6020e^{-10}$	$1.48e^{-10}$	$9.91e^{-08}$	$1.0e^{-10}$	96

Table 5: BR performance for Brownian motion parameter Nb

BR once again records very similar low performance errors (down to 10−12). Effective parameter counts remain moderate, and sum-squared parameter values remain low, again establishing negligible overfitting. All these indicators affirm the high quality of BR in learning Brownian motion behavior

appropriately.

Table 5. Performance metrics of ANN using Bayesian Regularization (BR) for Brownian motion parameter Nb, with effective parameters and regularization stats.

Nb	Training	Validation	Test	Performance	Gradient	Mu	Epoch	Effective # Param	Sum Squared Param
0.1	$1.2152e^{-12}$	NaN	$1.3113e^{-12}$	$1.22e^{-11}$	$9.9e^{-08}$	$5e^{03}$	252	22.2	372
0.2	$2.5731e^{-11}$	NaN	$6.6441e^{-11}$	$2.57e^{-11}$	$1.25e^{-07}$	$5e^{03}$	1000	11.7	116
0.3	$7.6694e^{-12}$	NaN	$6.6765e^{-12}$	$7.67e^{-12}$	$1.92e^{-08}$	$5e^{04}$	131	19.2	142

Table 6: SCG performance for Brownian motion parameter Nb

SCG (10−5) performance errors are significantly higher than those of LM and BR. The method has moderate Nb variability and exhibits poor learning. Its faster training comes at the cost of accuracy, as would be expected with gradient-based methods that do not include strong regularization.

Table 6. ANN performance using Scaled Conjugate Gradient (SCG) for various Nb values.

Nb	Training	Validation	Test	Performance	Gradient	Mu	Epoch
0.1	$3.3052e^{-05}$	$1.9886e^{-05}$	$4.0431e^{-05}$	$3.12e^{-05}$	$7.55e^{-05}$	---	61
0.2	$2.0090e^{-05}$	$1.8031e^{-05}$	$2.1100e^{-05}$	$1.97e^{-05}$	$8.99e^{-05}$	---	166
0.3	$2.9799e^{-05}$	$3.0584e^{-05}$	$3.0689e^{-05}$	$2.88e^{-05}$	$3.92e^{-05}$	---	84

Table 7: LM performance for thermophoresis parameter Nt

LM has satisfactory performance (10−10), with convergence within less than 500 epochs. Highly minimal variation across training, validation, and test errors supports model stability. The strategy performs satisfactorily for all values of Nt.

Table 7. ANN results using Levenberg–Marquardt (LM) for different values of thermophoresis parameter Nt.

Nt	Training	Validation	Test	Performance	Gradient	Mu	Epoch
0.1	$2.1951e^{-10}$	$2.3847e^{-10}$	$2.3141e^{-10}$	$2.20e^{-10}$	$9.92e^{-08}$	$1.0e^{-08}$	426
0.2	$2.4176e^{-10}$	$2.7161e^{-10}$	$2.4276e^{-10}$	$2.42e^{-10}$	$8.62e^{-08}$	$1.0e^{-10}$	220
0.3	$8.3116e^{-11}$	$8.7440e^{-11}$	$7.8181e^{-11}$	$8.31e^{-11}$	$9.81e^{-08}$	$1.0e^{-09}$	357

Table 8: BR performance for thermophoresis parameter Nt

BR offers very low errors (10−13 to 10−12) and consistent values for gradient and epochs. It keeps the well-organized network size with low counts of parameters well below 170 that maintain computational efficiency along with accuracy. It is still the best performer.

Table 8. Performance of ANN using Bayesian Regularization (BR) for thermophoresis parameter Nt, including network complexity details.

Nt	Training	Validation	Test	Performance	Gradient	Mu	Epoch	Effective # Param	Sum Squared Param
0.1	$3.0463e^{-13}$	NaN	$3.4962e^{-13}$	$3.05e^{-13}$	$8.97e^{-09}$	$5e^{04}$	168	25.7	220
0.2	$8.1055e^{-13}$	NaN	$9.4662e^{-13}$	$8.11e^{-13}$	$1.52e^{-08}$	$5e^{04}$	154	24.3	177
0.3	$6.2631e^{-12}$	NaN	$7.6375e^{-12}$	$6.26e^{-12}$	$5.05e^{-08}$	$5e^{03}$	101	26.7	285

Table 9: SCG performance for thermophoresis parameter Nt

SCG produces more errors (10−5 to 10−4) compared to LM and BR. Results are expected but non-competitive accuracy-wise. While quickly trainable, SCG is not strong in accurately predicting thermophoretic effects.

Table 9. Results of ANN training using Scaled Conjugate Gradient (SCG) for various thermophoresis parameter Nt values.

Nt	Training	Validation	Test	Performance	Gradient	Mu	Epoch
0.1	$7.7012e^{-05}$	$5.7783e^{-05}$	$9.9583e^{-05}$	$7.03e^{-05}$	$5.58e^{-05}$	---	34
0.2	$7.1330e^{-05}$	$7.9822e^{-05}$	$7.7601e^{-05}$	$6.99e^{-05}$	$4.53e^{-05}$	---	75
0.3	$7.5764e^{-05}$	$6.0966e^{-05}$	$6.9896e^{-05}$	$7.46e^{-05}$	$6.71e^{-05}$	---	100

Table 10: LM performance for bioconvection Lewis number Lb

LM performance remains 10−9 to 10−12 with stable gradients and good convergence. The algorithm performs satisfactorily for any Lb value without any notable sign of instability or overfitting.

Table 10. ANN performance using Levenberg–Marquardt (LM) for varying values of bioconvection Lewis number Lb.

Lb	Training	Validation	Test	Performance	Gradient	Mu	Epoch
1.0	$1.3556e^{-09}$	$1.4253e^{-09}$	$1.4529e^{-09}$	$1.36e^{-09}$	$1.00e^{-07}$	$1.0e^{-08}$	195
2.0	$9.6931e^{-12}$	$1.0510e^{-11}$	$9.2822e^{-12}$	$9.69e^{-12}$	$5.26e^{-08}$	$1.0e^{-10}$	242
3.0	$3.0100e^{-10}$	$4.0550e^{-10}$	$3.5604e^{-10}$	$3.01e^{-10}$	$9.97e^{-08}$	$1.0e^{-10}$	199

Table 11: Bioconvection Lewis number Lb performance for BR

BR again performs better, with consistently low performance measures and perfect convergence. Useful parameter numbers are slightly higher in this scenario, a sign of complex patterns well represented in the Lb-sensitive ANN models. The method shows strong generalization for all possible values of Lewis number.

Table 11. Performance metrics of ANN using Bayesian Regularization (BR) for Lb, including effective parameter count and sum-squared weights.

Lb	Training	Validation	Test	Performance	Gradient	Mu	Epoch	Effective # Param	Sum Squared Param
1.0	$5.1326e^{-11}$	NaN	$4.9929e^{-11}$	$5.13e^{-11}$	$9.99e^{-08}$	$5e^{03}$	474	26.4	588
2.0	$6.5100e^{-11}$	NaN	$7.8212e^{-11}$	$6.51e^{-11}$	$9.93e^{-08}$	$5e^{03}$	223	28.1	658
3.0	$1.0292e^{-11}$	NaN	$7.8766e^{-12}$	$1.03e^{-11}$	$9.88e^{-08}$	$5e^{03}$	167	27.5	570

Table 12: SCG performance for bioconvection Lewis number Lb

SCG exhibits huge error oscillations with Lb value variations, especially with Lb=2.0, where errors skyrocket. This inconsistency attests to unreliability when handling bioconvection parameters. Even though computationally inexpensive, SCG is clearly the least reliable under such circumstances.

Table 12. ANN results using Scaled Conjugate Gradient (SCG) for different Lb values.

Lb	Training	Validation	Test	Performance	Gradient	Mu	Epoch
1.0	$2.8270e^{-05}$	$2.8264e^{-05}$	$2.9981e^{-05}$	$2.62e^{-05}$	$1.71e^{-05}$	---	74
2.0	$2.0423e^{-04}$	$2.1420e^{-04}$	$2.6591e^{-04}$	$1.21e^{-04}$	$2.30e^{-04}$	---	69
3.0	$1.7697e^{-05}$	$1.4258e^{-05}$	$1.1924e^{-05}$	$1.65e^{-05}$	$2.17e^{-05}$	---	60

5. Conclusions

This review critically analyzed the use of ANNs to simulate complex MHD hybrid nanofluid flows, particularly those with bioconvection and internally heat-source driven. Focus was applied on three well-known training algorithms LM, BR, and SCG. The comparative assessment demonstrates the ability of ANN-based models to simulate nonlinear thermal and flow behavior properly with robust generalization, reduced residual errors, and reduced computation. It bridges the gap between traditional numerical approaches and smart data-driven approaches in complicated fluid dynamics.

Key findings:

- Levenberg–Marquardt (LM) algorithm obtained the lowest prediction error and fastest convergence and was therefore the most accurate for MHD hybrid nanofluid simulations.
- Bayesian Regularization (BR) generalized better to unseen data and was therefore best for cases involving possible overfitting or noisy experimental data.
- Scaled Conjugate Gradient (SCG) had faster training time but relatively larger error variance, indicating a tradeoff between speed and predictability stability.
- ANN adequately captured nonlinear interactions among input parameters such as magnetic field intensity (M), Brownian movement (Nb), thermophoresis (Nt), and bioconvective Lewis number (Lb).
- Actual versus predicted output contour plots and surface plots confirmed high correlation and low spatial prediction error across the computational domain.

- Residual plots, like histograms and KDE (Kernel Density Estimate) curves, captured a near-Gaussian distribution around zero, reflecting minimal model bias.
- 3D surface plots took hold of uniform prediction across complex regions, affirming the ANN's ability to interpolate within high-dimensional nonlinear flow patterns.
- The confidence band vs. prediction plot demonstrated that an overwhelming majority of predicted values fall under a tight confidence band, indicating model solidity.
- Hexbin plots and violin plots illustrated tight concentration of predictions around real values, particularly with LM training.
- SOM analysis graphically visualized the distribution of weight learned positions and their corresponding relationship to input-output clusters, with implications for learning behavior in the network.
- UMAP and PCA projections unveiled unique patterns of clustering, confirming the dimensionality reduction ability and preservation of meaningful nonlinear relationships in the dataset by the ANN.
- The contour plot of the error surface and heatmap of mean error plotted spatial regions with least and highest deviations, facilitating interpretability of the model.
- Residuals vs. predicted values showed symmetric, homoscedastic spread with no apparent systematic error pattern.
- CPU time analysis indicated that ANN methods considerably reduced computation effort in comparison to conventional iterative solvers of fluid models.
- Parallel coordinate plots highlighted the impact of single input parameter on the network prediction response, allowing for feature sensitivity testing.
- Bifurcation plots vs. magnetic parameter (M) indicated critical transitions and model flexibility in nonlinear flow regimes.
- Nonlinear polynomial regression and scatter-plots validated high linear and nonlinear correlation between the actual and ANN-predicted outputs.
- The ANN interpolated output contour also closely tracked physics-based numerical simulations, illustrating the spatial generalization precision of the model.
- Correlation heatmaps validated high linear correlations between selected input and output parameters, validating further ANN model validation.
- Our analysis also took robustness and interpretability into account and showed that BR is not only more accurate but also more perturbation-stable and yields interpretable feature attribution and therefore adheres to the safe ML paradigm.

All things considered, the disparities in ANN training techniques show shocking compromises between computing power and prediction accuracy. The Levenberg-Marquardt algorithm may be susceptible to overfitting when it is near exceptionally nonlinear zones, even though it has a low CPU time and a respectably high rate of convergence. Bayesian Normalization is more precise and robust to noisy input, and converges more steadily, even though it costs a little more to compute. Compared to LM and BR, the SCG is less complicated and requires less memory, but is less precise and less convergent. These findings collectively show that BR is the most stable when precision and stability are most important, LM is appropriate for quick estimations, and SCG should only be used when memory issues are of utmost importance.

Author contributions

Sohaib Abdal: writing-original draft, methodology, formal analysis. Adnan Ashique: resources, validation, funding acquisition; Usman Afzal: writing-original draft, software; Maddina Dinesh Kumar: writing-review and editing, formal analysis, conceptualization; Khalid Masood: resources, methodology, software, project administration; Nehad Ali Shah: writing-review and editing, supervision. Sohaib Abdal and Nehad Ali Shah contributed equally to this work and are co-first authors. All authors have read and approved the final version of the manuscript for publication.

Use of Generative-AI tools declaration

The authors declare they have not used Artificial Intelligence (AI) tools in the creation of this article.

Conflict of interest

The authors declare no conflicts of interest.

References

1. N. A. M. Alkuhayli, Heat transfer analysis of a hybrid nanofluid flow on a rotating disk considering thermal radiation effects, *Case Stud. Therm. Eng.*, **49** (2023), 103131. https://doi.org/10.1016/j.csite.2023.103131
2. B. Venkateswarlu, P. V. S. Narayana, A. J. Chamkha, Heat energy impacts on hybrid (copper-titanium/water) nanofluid flow over a porous elongated sheet, *J. Nanofluids*, **13** (2024), 863–872. https://doi.org/10.1166/jon.2024.2181
3. S. Ontela, P. K. Pattnaik, S. Panda, S. R. Mishra, Optimizing heat transfer rate and sensitivity analysis of hybrid nanofluid flow over a radiating sheet: applications in solar-powered charging stations, *Numer. Heat Tr. B-Fund.*, **2024** (2024), 1–21. https://doi.org/10.1080/10407790.2024.2341439
4. M. Atashafrooz, H. Sajjadi, A. A. Delouei, Simulation of combined convective-radiative heat transfer of hybrid nanofluid flow inside an open trapezoidal enclosure considering magnetic force impacts, *J. Magn. Magn. Mater.*, **567** (2023), 170354. https://doi.org/10.1016/j.jmmm.2023.170354
5. W. Al-Kouz, W. Owhaib, A. Ayub, B. Souayeh, M. Hader, R. Z. Homod, et al., Thermal proficiency of magnetized and radiative cross-ternary hybrid nanofluid flow induced by a vertical cylinder, *Open Phys.*, **22** (2024), 20230197. https://doi.org/10.1515/phys-2023-0197
6. A. U. Awan, B. Ali, S. A. A. Shah, M. Oreijah, K. Guedri, S. M. Eldin, Numerical analysis of heat transfer in Ellis hybrid nanofluid flow subject to a stretching cylinder, *Case Stud. Therm. Eng.*, **49** (2023), 103222. https://doi.org/10.1016/j.csite.2023.103222
7. M. Qayyum, S. Afzal, S. T. Saeed, A. Akgül, M. B. Riaz, Unsteady hybrid nanofluid (Cu-UO_2/blood) with chemical reaction and non-linear thermal radiation through convective boundaries: An application to bio-medicine, *Heliyon*, **9** (2023), e16578. https://doi.org/10.1016/j.heliyon.2023.e16578

8. N. Sandeep, B. Ranjana, C. Sulochana, G. P. Ashwinkumar, Flow and heat transfer mechanism of engine-oil based hybrid nanofluid due to a nonlinearly extending surface: A comparative study, *International Journal of Modelling and Simulation*, **45** (2025), 665–681. https://doi.org/10.1080/02286203.2023.2235539
9. P. S. Reddy, P. Sreedevi, A. J. Chamkha, Hybrid nanofluid heat and mass transfer characteristics over a stretching/shrinking sheet with slip effects, *J. Nanofluids*, **12** (2023), 251–260. https://doi.org/10.1166/jon.2023.1996
10. U. Farooq, M. Imran, N. Fatima, S. Noreen, M. Tahir, A. Akgül, et al., Cattaneo–Christov heat flux model in radiative flow of (Fe_3O_4-TiO_2/transformer oil) and (Cu-TiO_2/transformer oil) magnetized hybrid nanofluids past double rotating disks, *Case Stud. Therm. Eng.*, **45** (2023), 102905. https://doi.org/10.1016/j.csite.2023.102905
11. S. G. Li, R. Saadeh, J. K. Madhukesh, U. Khan, G. K. Ramesh, A. Zaib, et al., Aspects of an induced magnetic field utilization for heat and mass transfer ferromagnetic hybrid nanofluid flow driven by pollutant concentration, *Case Stud. Therm. Eng.*, **53** (2024), 103892. https://doi.org/10.1016/j.csite.2023.103892
12. Y. Ouyang, M. F. M. Basir, K. Naganthran, I. Pop, Effects of discharge concentration and convective boundary conditions on unsteady hybrid nanofluid flow in a porous medium, *Case Stud. Therm. Eng.*, **58** (2024), 104374. https://doi.org/10.1016/j.csite.2024.104374
13. E. A. Algehyne, Z. Raizah, T. Gul, A. Saeed, S. M. Eldin, A. M. Galal, Cu and Al_2O_3-based hybrid nanofluid flow through a porous cavity, *Nanotechnol. Rev.*, **12** (2023), 20220526. https://doi.org/10.1515/ntrev-2022-0526
14. T. Gul, S. Nasir, A. S. Berrouk, Z. Raizah, W. Alghamdi, I. Ali, et al., Simulation of water-based hybrid nanofluids flow through a porous cavity for heat transfer applications, *Sci. Rep.*, **13** (2023), 7009. https://doi.org/10.1038/s41598-023-33650-w
15. A. Paul, J. M. Nath, T. K. Das, An investigation of the MHD Cu-Al_2O_3/H_2O hybrid-nanofluid in a porous medium across a vertically stretching cylinder incorporating thermal stratification impact, *J. Ther. Eng.*, **9** (2023), 799–810.
16. M. Ismail, D. M. Gururaj, Numerical investigation on nonlinear radiative magnetohydrodynamics hybrid nanofluid flow past a stretching cylinder embedded in a porous medium, *J. Nanofluids*, **12** (2023), 809–818. https://doi.org/10.1166/jon.2023.1962
17. D. Z. Yang, S. Ahmad, K. Ali, S. Algarni, T. Alqahtani, W. Jamshed, et al., CFD analysis of paraffin-based hybrid (Co-Au) and trihybrid (Co-Au-ZrO_2) nanofluid flow through a porous medium, *Nanotechnol. Rev.*, **13** (2024), 20240024. https://doi.org/10.1515/ntrev-2024-0024
18. M. A. Memon, K. Jacob, H. B. Lanjwani, E. E. Mahmoud, Darcy–Forchheimer MHD micropolar water-based hybrid nanofluid flow, heat and mass transfer past a stretching/shrinking surface with slip and radiation effects, *Results in Engineering*, **23** (2024), 102534. https://doi.org/10.1016/j.rineng.2024.102534
19. F. H. Sohut, U. Khan, A. Ishak, S. K. Soid, I. Waini, Mixed convection hybrid nanofluid flow induced by an inclined cylinder with Lorentz forces, *Micromachines*, **14** (2023), 982. https://doi.org/10.3390/mi14050982
20. K. Rafique, Z. Mahmood, Adnan, U. Khan, U. Farooq, W. Emam, Computational analysis of MHD hybrid nanofluid over an inclined cylinder: variable thermal conductivity and viscosity with buoyancy and radiation effects, *Mod. Phys. Lett. B*, **39** (2025), 2550033. https://doi.org/10.1142/S0217984925500332

21. G. Rasool, A. Wakif, X. H. Wang, A. Alshehri, A. M. Saeed, Falkner–Skan aspects of a radiating (50% ethylene glycol + 50% water)-based hybrid nanofluid under Joule heating with Darcy–Forchheimer and Lorentz forces, *Propuls. Power Res.*, **12** (2023), 428–442. https://doi.org/10.1016/j.jppr.2023.07.001
22. T. Sajid, S. Algarni, H. Ahmad, T. Alqahtani, W. Jamshed, M. R. Eid, et al., Exploration of irreversibility process and thermal energy of a tetra-hybrid radiative binary nanofluid focusing on solar implementations, *Nanotechnol. Rev.*, **13** (2024), 20240040. https://doi.org/10.1515/ntrev-2024-0040
23. A. Sarkar, K. Das, Magneto hybrid nanofluid flow with activation energy and chemical reaction through an impermeable stretching elastic cylinder, *International Journal of Modelling and Simulation*, **2023** (2023), 1–13. https://doi.org/10.1080/02286203.2023.2296264
24. P. Guo, Y. C. Leng, F. Nazir, J. Ahmed, A. Mohamed, I. Khan, I. E. Elseesy, Mixed convection phenomenon for hybrid nanofluid flow exterior to a vertical spinning cylinder with binary chemical reaction and activation energy, *Case Stud. Therm. Eng.*, **54** (2024), 103943. https://doi.org/10.1016/j.csite.2023.103943
25. A. Abd-Elmonem, S. Kanwal, M. Imtiaz, K. Ali, S. Ahmad, W. Jamshed, et al., Case study of heat generation/absorption and activation energy on MHD hybrid nanofluid (GO-MoS2/water) flow owing to a rotatfing disk, *Case Stud. Therm. Eng.*, **51** (2023), 103632. https://doi.org/10.1016/j.csite.2023.103632
26. F. Haq, H. A. Ghazwani, J. Younis, M. H. Ghazwani, A. Alnujaie, Numerical investigation of mass and heat transfer in ternary hybrid nanofluid flow with activation energy, *Int. J. Energ. Res.*, **2025** (2025), 8061691. https://doi.org/10.1155/er/8061691
27. S. Ahmed, Z.-M. Chen, M. Ishaq, Multiple solutions in magnetohydrodynamic stagnation flow of hybrid nanofluid past a sheet with chemical reaction model and stability analysis, *Phys. Fluids*, **35** (2023), 072002. https://doi.org/10.1063/5.0157429
28. J. Manigandan, D. Iranian, I. Khan, N. A. Mohammed, H. Alhazmi, Numerical simulations of thermal heat conservation in hybrid nanofluids with chemical reaction, viscous dissipation, and inclination, *Case Stud. Therm. Eng.*, **58** (2024), 104386. https://doi.org/10.1016/j.csite.2024.104386
29. S. Khalatbari, P. Jalili, B. Jalili, D. D. Ganji, Investigating the improvement of heat transfer and flow characteristics of hybrid nanofluids: A comprehensive review, *P. I. Mech. Eng. E.-J. Pro.*, **2025** (2025), 09544089251318785. https://doi.org/10.1177/09544089251318785
30. M. Abbas, N. Khan, M. S. Hashmi, J. Younis, Numerical analysis of Marangoni convective flow of hybrid nanofluid over an infinite disk with thermophoresis particle deposition, *Sci. Rep.*, **13** (2023), 5036. https://doi.org/10.1038/s41598-023-32011-x
31. H. B. Marulasiddeshi, P. K. Kanti, S. B. Prakash, S. N. Sridhara, Investigation of entropy generation and thermohydraulic characteristics of Al2O3-CuO hybrid nanofluid flow in a pipe at different inlet fluid temperatures, *Int. J. Therm. Sci.*, **193** (2023), 108541. https://doi.org/10.1016/j.ijthermalsci.2023.108541
32. Z. Mahmood, F. Z. Duraihem, Adnan, U. Khan, A. M. Hassan, Model-based comparative analysis of MHD stagnation point flow of hybrid nanofluid over a stretching sheet with suction and viscous dissipation, *Numer. Heat Tr. B-Fund.*, **86** (2025), 1639–1660. https://doi.org/10.1080/10407790.2024.2318457

33. T. Hayat, S. Amjad, Z. Nisar, A. Alsaedi, Analysis for peristaltic transport of MHD hybrid nanofluid with Darcy–Forchheimer porous medium, *Mod. Phys. Lett. B*, **39** (2025), 2550016. https://doi.org/10.1142/S0217984925500162
34. A. F. Alharbi, M. Alhawiti, M. Usman, I. Ullah, M. M. Alam, M. Bilal, Enhancement of heat transfer in thin-film flow of a hybrid nanofluid over an inclined rotating disk subject to thermal radiation and viscous dissipation, *Int. J. Heat Fluid Fl.*, **107** (2024), 109360. https://doi.org/10.1016/j.ijheatfluidflow.2024.109360
35. S. Saleem, B. Ahmad, A. Naseem, M. B. Riaz, T. Abbas, Mono and hybrid nanofluid analysis over shrinking surface with thermal radiation: a numerical approach, *Case Stud. Therm. Eng.*, **54** (2024), 104023. https://doi.org/10.1016/j.csite.2024.104023
36. K. Abbas, X. H. Wang, G. Rasool, T. Sun, I. Razzaq, Thermal optimization of buoyancy driven radiative engine-oil based viscous hybrid nanofluid flow observing micro-rotations in an inclined permeable enclosure, *Case Stud. Therm. Eng.*, **60** (2024), 104774. https://doi.org/10.1016/j.csite.2024.104774
37. E. Elfiano, N. M. I. N. Ibrahim, M. K. A. Mohamed, Mixed convection boundary layer flow on a vertical flat plate in Al2O3-Ag/water hybrid nanofluid with viscous dissipation effects, *Journal of Advanced Research in Numerical Heat Transfer*, **22** (2024), 1–13. https://doi.org/10.37934/arnht.22.1.113
38. A. Tulu, L. Asefa, M. Sohail, Unsteady magnetohydrodynamic hybrid nanofluid flow over a rotating disk with viscous dissipation and Cattaneo–Christov heat flux model, *International Journal of Thermofluids*, **21** (2024), 100586. https://doi.org/10.1016/j.ijft.2024.100586
39. A. Rehman, D. Khan, I. Mahariq, M. A. Elkotb, T. Elnaqeeb, Viscous dissipation effects on time-dependent MHD Casson nanofluid over a stretching surface: A hybrid nanofluid study, *J. Mol. Liq.*, **408** (2024), 125370. https://doi.org/10.1016/j.molliq.2024.125370
40. S. R. Mishra, S. Panda, R. Baithalu, Enhanced heat transfer rate on the flow of hybrid nanofluid through a rotating vertical cone: a statistical analysis, *Partial Differential Equations in Applied Mathematics*, **11** (2024), 100825. https://doi.org/10.1016/j.padiff.2024.100825
41. P. Choudhary, S. Choudhary, K. Jat, K. Loganathan, S. Eswaramoorthi, Impacts of unsteady MHD hybrid nanofluid over a non-linear stretchable porous sheet with thermal radiation and gyrotactic microorganisms, *International Journal of Thermofluids*, **23** (2024), 100788. https://doi.org/10.1016/j.ijft.2024.100788
42. R. M. Ramana, C. Maheswari, S. M. Shaw, G. Dharmaiah, U. Fernandez-Gamiz, S. Noeiaghdam, Numerical investigation of 3-D rotating hybrid nanofluid Forchheimer flow with radiation absorption over a stretching sheet, *Results in Engineering*, **22** (2024), 102019. https://doi.org/10.1016/j.rineng.2023.102019
43. S. M. R. S. Naqvi, U. Manzoor, H. Waqas, D. Liu, H. Naeem, S. M. Eldin, et al., Numerical investigation of thermal radiation with entropy generation effects in hybrid nanofluid flow over a shrinking/stretching sheet, *Nanotechnol. Rev.*, **13** (2024), 20230171. https://doi.org/10.1515/ntrev-2023-0171
44. J. Madhu, J. K. Madhukesh, I. Sarris, B. C. Prasannakumara, G. K. Ramesh, N. A. Shah, et al., Influence of quadratic thermal radiation and activation energy impacts over oblique stagnation point hybrid nanofluid flow across a cylinder, *Case Stud. Therm. Eng.*, **60** (2024), 104624. https://doi.org/10.1016/j.csite.2024.104624

45. M. Z. Bani-Fwaz, Adnan, S. U. Khan, B. S. Goud, T. Walelign, K. K. Asogwa, et al., Thermal performance of Falkner–Skan model (FSM) for (GO-MoS_2)/($C_2H_6O_2$-H_2O) 50:50% nanofluid under radiation heating source, *Sci. Rep.*, **15** (2025), 3885. https://doi.org/10.1038/s41598-025-86470-5
46. A. Ezhilarasi, D. Mohanavel, Heat transfer and sensitivity exploration of gyrotactic microorganisms suspended in a Casson hybrid nanofluid flow on a permeable stenosed artery, *Phys. Fluids*, **37** (2025), 021925. https://doi.org/10.1063/5.0254303
47. K. Thirumalaisamy, Y. D. Lee, H. Kim, Magnetohydrodynamic buoyancy-driven hybrid nanofluid flow and heat transfer within a partially heated porous square cavity, *Phys. Fluids*, **37** (2025), 042011. https://doi.org/10.1063/5.0264031
48. A. Kumar, B. K. Sharma, B. Almohsen, L. M. Pérez, K. Urbanowicz, Artificial neural network analysis of Jeffrey hybrid nanofluid with gyrotactic microorganisms for optimizing solar thermal collector efficiency, *Sci. Rep.*, **15** (2025), 4729. https://doi.org/10.1038/s41598-025-88877-6
49. M. A. Almeshaal, 3D convective flow in a hybrid nanofluid filled bi-truncated-pyramid equipped with adiabatic cylinders, *Front. Chem.*, **12** (2024), 1522372. https://doi.org/10.3389/fchem.2024.1522372
50. T. Hai, A. Basem, A. Alizadeh, P. K. Singh, H. Rajab, C. Maatki, et al., Optimizing ternary hybrid nanofluids using neural networks, gene expression programming, and multi-objective particle swarm optimization: A computational intelligence strategy, *Sci. Rep.*, **15** (2025), 1986. https://doi.org/10.1038/s41598-025-85236-3
51. A. M. Hassaan, Evaluating experimentally the viability of employing hybrid nanofluids as an operating fluid in a shell-and-tube heat exchanger, *Sci. Rep.*, **15** (2025), 4030. https://doi.org/10.1038/s41598-025-87149-7
52. Z. H. Khan, W. A. Khan, S. M. Ibrahim, K. Swain, Z. T. Huang, Impact of multiple slips and thermal radiation on heat and mass transfer in MHD Maxwell hybrid nanofluid flow over porous stretching sheet, *Case Stud. Therm. Eng.*, **61** (2024), 104906. https://doi.org/10.1016/j.csite.2024.104906
53. V. J. Prajapati, R. Meher, Analysis of MHD tangent hyperbolic hybrid nanofluid flow with different base fluids over a porous stretched sheet, *J. Taibah Univ. Sci.*, **18** (2024), 2300851. https://doi.org/10.1080/16583655.2023.2300851
54. S. Sadighi, H. Afshar, M. Jabbari, H. A. D. Ashtiani, Heat and mass transfer for MHD nanofluid flow on a porous stretching sheet with prescribed boundary conditions, *Case Stud. Therm. Eng.*, **49** (2023), 103345. https://doi.org/10.1016/j.csite.2023.103345
55. M. Nazeer, M. W. Nazir, N. Ali, T. Javed, S. A. Abdelmohsen, M. I. Khan, Momentum and thermal transport analysis in MHD nanofluid through the thermally heated square conduit: finite element method, *J. Magn. Magn. Mater.*, **580** (2023), 170954. https://doi.org/10.1016/j.jmmm.2023.170954
56. R. M. Kumar, R. S. Raju, M. A. Kumar, Effects of chemical reaction, Soret and Dufour parameters on MHD dissipative Williamson nanofluid flow over a slippery stretching sheet through a porous medium, *International Journal of Modelling and Simulation*, **45** (2025), 1135–1145. https://doi.org/10.1080/02286203.2023.2261812
57. A. Asghar, A. F. Chandio, Z. Shah, N. Vrinceanu, W. Deebani, M. Shutaywi, et al., Magnetized mixed convection hybrid nanofluid with effect of heat generation/absorption and velocity slip condition, *Heliyon*, **9** (2023), e13189. https://doi.org/10.1016/j.heliyon.2023.e13189

58. I. Mechai, S. M. Alzahrani, H. A. Othman, S. H. Altoum, Z. Iqbal, A.-N. A.-H. Ahmad, et al., Nanomaterial heat transfer within thermal porous system in presence of Lorentz force, *Case Stud. Therm. Eng.*, **49** (2023), 103139. https://doi.org/10.1016/j.csite.2023.103139
59. Y. A. Rothan, Thermal management of nanofluid flow through porous container with impose of Lorentz force, *Case Stud. Therm. Eng.*, **60** (2024), 104779. https://doi.org/10.1016/j.csite.2024.104779
60. N. Vinodhini, V. R. Prasad, Numerical study of magneto-convective Buongiorno nanofluid flow in a rectangular enclosure under oblique magnetic field with heat generation/absorption and complex wall conditions, *Heliyon*, **9** (2023), e17669. https://doi.org/10.1016/j.heliyon.2023.e17669
61. B. Kumar, Prachi, A. Singhal, R. Nandkeolyar, P. Kumar, A. J. Chamkha, Regression analysis and features of negative activation energy for MHD nanofluid flow model: a comparative study, *Propuls. Power Res.*, **12** (2023), 273–283. https://doi.org/10.1016/j.jppr.2023.02.005
62. N. Tarakaramu, N. Sivakumar, N. Tamam, P. V. S. Narayana, S. Ramalingam, Theoretical analysis of Arrhenius activation energy on 3D MHD nanofluid flow with convective boundary condition, *Mod. Phys. Lett. B*, **38** (2024), 2341009. https://doi.org/10.1142/S0217984923410099
63. S. Jayanthi, H. Niranjan, Effects of Joule heating, viscous dissipation, and activation energy on nanofluid flow induced by MHD on a vertical surface, *Symmetry*, **15** (2023), 314. https://doi.org/10.3390/sym15020314
64. N. Vijay, K. Sharma, Magnetohydrodynamic hybrid nanofluid flow over a decelerating rotating disk with Soret and Dufour effects, Multidiscip, *Multidiscip. Model Ma.*, **19** (2023), 253–276. https://doi.org/10.1108/MMMS-08-2022-0160
65. J. Aruna, H. Niranjan, Effects of electric field, MHD micropolar hybrid nanofluid flow with mixed convection and thermal radiation across a flat surface, *J. Ther. Eng.*, **10** (2024), 1607–1620. https://doi.org/10.14744/thermal.0000851
66. M. G. Reddy, K. V. Reddy, B. Souayeh, H. Fayaz, Numerical entropy analysis of MHD electro-osmotic flow of peristaltic movement in a nanofluid, *Heliyon*, **10** (2024), e27185. https://doi.org/10.1016/j.heliyon.2024.e27185
67. S. Ijaz, M. Abdullah, H. Sadaf, S. Nadeem, Generalized complex cilia tip modeled flow through an electroosmotic region, *J. Cent. South Univ.*, **30** (2023), 1217–1230. https://doi.org/10.1007/s11771-023-5305-9
68. R. Gandhi, B. K. Sharma, N. K. Mishra, Q. M. Al-Mdallal, Computer simulations of EMHD Casson nanofluid flow of blood through an irregular stenotic permeable artery: application of Koo–Kleinstreuer–Li correlations, *Nanomaterials*, **13** (2023), 652. https://doi.org/10.3390/nano13040652
69. Z. Raizah, A. Khan, T. Gul, A. Saeed, E. Bonyah, A. M. Galal, Coupled Dufour and Soret effects on hybrid nanofluid flow through a gyrating channel subject to chemically reactive Arrhenius activation energy, *J. Nanomater.*, **2023** (2023), 9208703. https://doi.org/10.1155/2023/9208703
70. M. Prashanth, V. S. Rao, The impact of Soret, Dufour, and chemical reaction on MHD nanofluid over a stretching sheet, *Partial Differential Equations in Applied Mathematics*, **10** (2024), 100674. https://doi.org/10.1016/j.padiff.2024.100674
71. C. Maheswari, M. R. Ravuri, G. B. Prakash, D. Ramesh, D. V. Kumar, Influence of thermophoresis and Brownian motion on MHD hybrid nanofluid MgO-Ag/H_2O flow along moving slim needle, *Journal of Advanced Research in Applied Sciences and Engineering Technology*, **36** (2023), 67–90. https://doi.org/10.37934/araset.36.2.6790

72. A. H. Mirza, B. Dey, R. Choudhury, The detrimental effect of thermal exposure and thermophoresis on MHD flow with combined mass and heat transmission employing permeability, *International Journal of Applied Mechanics and Engineering*, **29** (2024), 90–104. https://doi.org/10.59441/ijame/181556
73. M. Priyadharsini, M. G. A. David, I. S. Mohammed, S. Mikhail, Numerical and sensitivity study on the heat transfer due to bioconvection on unsteady radiative MHD blood flow over a permeable artery with chemical reaction effects, *Int. Commun. Heat Mass*, **147** (2023), 106981. https://doi.org/10.1016/j.icheatmasstransfer.2023.106981
74. U. J. Das, N. M. Majumdar, I. Patgiri, Influence of thermophoretic deposition and viscous dissipation on magnetohydrodynamic flow with variable viscosity and thermal conductivity, *Heat Transf.*, **52** (2023), 4253–4273. https://doi.org/10.1002/htj.22875
75. M. Hasanuzzaman, S. Akter, S. Sharin, M. M. Hossain, A. Miyara, M. A. Hossain, Viscous dissipation effect on unsteady magneto-convective heat-mass transport passing in a vertical porous plate with thermal radiation, *Heliyon*, **9** (2023), e14207. https://doi.org/10.1016/j.heliyon.2023.e14207
76. D. Sahu, R. K. Deka, P. Das, R. Rabha, Comprehensive analysis of stratification and chemical reaction on MHD flow along an impulsively started infinite vertical plate in presence of radiation and heat source through porous medium, *Heat Transf.*, **54** (2025), 2645–2658. https://doi.org/10.1002/htj.23313
77. B. J. Dutta, B. Kalita, Effects of nonlinear thermal density variation and radiation on MHD mixed convection through a porous medium over a permeable vertical plate: A numerical approach, *Heat Transf.*, 54 (2025), 3163–3178. https://doi.org/10.1002/htj.23341
78. T. Maranna, U. S. Mahabaleshwar, H. N. Huang, S. W. Joo, An Analytical inspection on effect of chemical reaction and radiation on MHD biviscous Bingham tetra nanofluid flow with accelerated plate, *J. Nanotechnol.*, **2025** (2025), 1382579. https://doi.org/10.1155/jnt/1382579
79. C. Fetecau, S. Akhtar, N. C. Forna, C. Moroşanu, General solutions for MHD motions of second-grade fluids through a circular cylinder filled with porous medium, *Symmetry*, **17** (2025), 319. https://doi.org/10.3390/sym17030319
80. A. S. Negi, B. Kumar, A. Kumar, S. K. Rawat, M. Yaseen, Investigation of heat flux and heat source/sink effect on heat transfer ferrofluid ($CoFe_2O_4$-H_2O) flow in an induced magnetic field with porous medium within the horizontal channel, *Int. J. Ambient Energy*, **46** (2025), 2447939. https://doi.org/10.1080/01430750.2024.2447939
81. B. Ilias, A. Alahmer, A. Abderrahmane, O. Younes, S. Laoudj, R. Marzougi, Investigating flow and heat distribution of NE-PCM in a double lid-driven MHD octagonal chamber, *Heat Transf.*, **54** (2025), 2799–2815. https://doi.org/10.1002/htj.23325
82. P. K. Yadav, P. Srivastava, Brinkman–Forchheimer model of creeping flow of electromagnetohydrodynamic micropolar fluid through a swarm of cylindrical particles: cell model technique, *Phys. Fluids*, **37** (2025), 033104. https://doi.org/10.1063/5.0245425
83. V. B. R. Komaravolu, T. G. Rao, K. S. Balamurugan, C. B. Rani, Cross-diffusion effects on magnetohydrodynamic free convective flow over a vertical porous plate under the influence of chemical reactions, thermal radiation, and dissipative heating, *Heat Transf.*, **54** (2025), 3374–3391. https://doi.org/10.1002/htj.23358

84. B. Deka, R. Choudhury, Analysis of Soret and Dufour impacts on magnetohydrodynamics flow constrained between a long upright wavy wall and a parallel flat wall in a permeable medium, *Heat Transf.*, **54** (2025), 3973–3984. https://doi.org/10.1002/htj.23394
85. W. Aich, A. Abbas, A. M. Obalalu, W. Hassen, L. B. Said, R. Hajlaoui, L. Kolsi, Double diffusive MHD stagnation point flow of second grade fluid in non-Darcy porous media under radiation effects, *Sci. Rep.*, **15** (2025), 395. https://doi.org/10.1038/s41598-024-84562-2
86. J.-H. Pan, M.-J. Ni, Magnetohydrodynamic effects on liquid metal flows in an open channel for fusion plasma facing components with a transverse magnetic field, *Nucl. Fusion*, **65** (2025), 046015.
87. Y. J. Li, A. Majeed, N. Ijaz, K. Barghout, M. R. Ali, T. Muhammad, Melting thermal transportation in bioconvection Casson nanofluid flow over a nonlinear surface with motile microorganism: application in bioprocessing thermal engineering, *Case Stud. Therm. Eng.*, **49** (2023), 103285. https://doi.org/10.1016/j.csite.2023.103285
88. Z. M. Liu, S. G. Li, T. Sadaf, S. U. Khan, F. Alzahrani, M. I. Khan, et al., Numerical bio-convective assessment for rate type nanofluid influenced by Nield thermal constraints and distinct slip features, *Case Stud. Therm. Eng.*, **44** (2023), 102821. https://doi.org/10.1016/j.csite.2023.102821
89. G. Dharmaiah, F. Mebarek-Oudina, J. L. R. Prasad, C. B. Rani, Exploration of bio-convection for slippery two-phase Maxwell nanofluid past a vertical induced magnetic stretching regime associated for biotechnology and engineering, *J. Mol. Liq.*, **391** (2023), 123408. https://doi.org/10.1016/j.molliq.2023.123408
90. I. Tlili, T. A. Alkanhal, A. Rebey, M. B. Henda, S. E. A. Musmar, Nanofluid bioconvective transport for non-Newtonian material in bidirectional oscillating regime with nonlinear radiation and external heat source: applications to storage and renewable energy, *J. Energy Storage*, **68** (2023), 107839. https://doi.org/10.1016/j.est.2023.107839
91. A. S. M. Aljaloud, L. Manai, I. Tlili, Bioconvection flow of Cross nanofluid due to cylinder with activation energy and second order slip features, *Case Stud. Therm. Eng.*, **42** (2023), 102767. https://doi.org/10.1016/j.csite.2023.102767
92. V. Makkar, V. Poply, N. Sharma, Three-dimensional modelling of magnetohydrodynamic bio-convective Casson nanofluid flow with buoyancy effects over exponential stretching sheet along with heat source & gyrotactic micro-organisms, *J. Nanofluids*, **12** (2023), 535–547. https://doi.org/10.1166/jon.2023.1921
93. P. M. Patil, S. Benawadi, The bioconvective flow of an Eyring–Powell nanoliquid: the influence of entropy, *International Journal of Modelling and Simulation*, **45** (2025), 405–419. https://doi.org/10.1080/02286203.2023.2205988
94. A. Hussain, S. Riaz, A. Hassan, M. Y. Malik, A. S. Alqahtani, H. Karamti, et al., Magneto-bio-convection enhanced heat transfer in Prandtl hybrid nanofluid with inclined magnetization and microorganism migration, *J. Magn. Magn. Mater.*, **588** (2023), 171403. https://doi.org/10.1016/j.jmmm.2023.171403
95. M. Ali, M. Tabrez, H. Liu, W. A. Khan, Magnetized bioconvective thermal efficacy of ferromagnetic nanoparticles involving appliance of radiation and viscous dissipation, *Thermal Science and Engineering Progress*, **47** (2024), 102314. https://doi.org/10.1016/j.tsep.2023.102314
96. I. Hussain, W. A. Khan, M. Tabrez, M. Ali, M. Waqas, I. Boukhris, et al., Bioconvection aspects in magnetized Eyring–Powell fluid configured by suspension of ferromagnetic nanoparticles subject to gyrotactic moment of microorganisms, *Tribol. Int.*, **189** (2023), 108876. https://doi.org/10.1016/j.triboint.2023.108876

97. M. I. Kopp, V. V. Yanovsky, Effect of gravity modulation on weakly nonlinear bio-thermal convection in a porous medium layer, *J. Appl. Phys.*, **134** (2023), 104702. https://doi.org/10.1063/5.0165178
98. S. Rehman, S. Bouzgarrou, Hashim, M. H. dhaou, M. Boujelbene, Darcy–Forchheimer flow of bioconvective nanofluid over a nonaligned stretching surface with slip effects, *Mater. Today Commun.*, **37** (2023), 107444. https://doi.org/10.1016/j.mtcomm.2023.107444
99. K. M. Nihaal, U. S. Mahabaleshwar, S. W. Joo, Darcy–Forchheimer imposed exponential heat source-sink and activation energy with the effects of bioconvection over radially stretching disc, *Sci. Rep.*, **14** (2024), 7910. https://doi.org/10.1038/s41598-024-58051-5
100. M. S. Alqurashi, U. Farooq, M. Sediqmal, H. Waqas, S. Noreen, M. Imran, et al., Significance of melting heat in bioconvection flow of micropolar nanofluid over an oscillating surface, *Sci. Rep.*, **13** (2023), 11692. https://doi.org/10.1038/s41598-023-38361-w
101. B. C. Prasannakumara, J. K. Madhukesh, G. K. Ramesh, Bioconvective nanofluid flow over an exponential stretched sheet with thermophoretic particle deposition, *Propuls. Power Res.*, **12** (2023), 284–296. https://doi.org/10.1016/j.jppr.2023.05.004
102. Y.-M. Chu, S. Jakeer, S. R. R. Reddy, M. L. Rupa, Y. Trabelsi, M. I. Khan, et al., Double diffusion effect on the bio-convective magnetized flow of tangent hyperbolic liquid by a stretched nano-material with Arrhenius catalysts, *Case Stud. Therm. Eng.*, **44** (2023), 102838. https://doi.org/10.1016/j.csite.2023.102838
103. L. Kolsi, K. Al-Khaled, S. U. Khan, N. B. Khedher, Effect of thermal radiation and variable viscosity on bioconvective and thermal stability of non-Newtonian nanofluids under bidirectional porous oscillating regime, *Mathematics*, **11** (2023), 1600. https://doi.org/10.3390/math11071600
104. F. Peter, P. Sambath, S. Dhanasekaran, Analyzing the MHD bioconvective Eyring–Powell fluid flow over an upright cone/plate surface in a porous medium with activation energy and viscous dissipation, *Computation*, **12** (2024), 48. https://doi.org/10.3390/computation12030048
105. M. I. Khan, F. Shah, S. S. Abdullaev, S. G. Li, R. Altuijri, H. Vaidya, et al., Heat and mass transport behavior in bio-convective reactive flow of nanomaterials with Soret and Dufour characteristics, *Case Stud. Therm. Eng.*, **49** (2023), 103347. https://doi.org/10.1016/j.csite.2023.103347
106. W. Ibrahim, T. Gizewu, Analysis of entropy generation of bio-convection on curved stretching surface with gyrotactic micro-organisms and third-order slip flow, *International Journal of Thermofluids*, **17** (2023), 100277. https://doi.org/10.1016/j.ijft.2022.100277
107. D. Das, S. Shaw, R. R. Kairi, Irreversibility estimation in triply stratified bio-Marangoni convection in Powell–Eyring nanofluid under the influence of external flow, *Phys. Scripta*, **99** (2024), 055253.
108. B. Arun, M. Deivanayaki, S. K. Vaithilingam, Bioconvection flow in the presence of Casson nanoparticles on a stretching/shrinking vertical sheet with chemical reaction, *J. Chem.*, **2023** (2023), 6199200. https://doi.org/10.1155/2023/6199200
109. N. A. Shah, F. Ali, M. Faizan, S. S. Zafar, Theoretical exploration of bioconvection magneto flow of micropolar nanomaterial off-centered stagnation point framed by rotating disk, *Adv. Theor. Simul.*, **8** (2025), 2401345. https://doi.org/10.1002/adts.202401345
110. S. Jakeer, S. R. R. Reddy, S. V. Easwaramoorthy, H. T. Basha, J. Cho, Influence of induced magnetic fields and double-diffusive convection on Carreau nanofluid flow through diverse geometries: numerical and ANN approaches, *Mathematics*, **11** (2023), 3687. https://doi.org/10.3390/math11173687

111. A. Basu, A. Saha, S. Banerjee, P. C. Roy, B. Kundu, A review of artificial intelligence methods in predicting thermophysical properties of nanofluids for heat transfer applications, *Energies*, **17** (2024), 1351. https://doi.org/10.3390/en17061351
112. A. Alotaibi, T. Gul, I. M. S. Alotaibi, A. Alghuried, A. S. Alshomrani, M. Alghuson, Artificial neural network analysis of the flow of nanofluids in a variable porous gap between two inclined cylinders for solar applications, *Eng. Appl. Comp. Fluid*, **18** (2024), 2343418. https://doi.org/10.1080/19942060.2024.2343418
113. M. D. Shamshuddin, S. O. Salawu, K. K. Asogwa, P. S. Rao, Thermal exploration of convective transportation of ethylene glycol-based magnetized nanofluid flow in porous cylindrical annulus utilizing MoS_2 and Fe_3O_4 nanoparticles with inconstant viscosity, *J. Magn. Magn. Mater.*, **573** (2023), 170663. https://doi.org/10.1016/j.jmmm.2023.170663
114. M. N. Hudha, M. J. Hasan, T. Bairagi, A. K. Azad, M. M. Rahman, Artificial neural network analysis on the effect of mixed convection in triangular-shaped geometry using water-based Al2O3 nanofluid, *PLoS One*, **19** (2024), e0304826. https://doi.org/10.1371/journal.pone.0304826
115. H. A. Prince, A. Ghosh, M. M. H. Siam, M. A. H. Mamun, AI predicts MHD double-diffusive mixed convection and entropy generation in hybrid nanofluids for different magnetic field inclination angles by ANN, *International Journal of Thermofluids*, **19** (2023), 100383. https://doi.org/10.1016/j.ijft.2023.100383
116. P. Chinnasamy, R. Sivajothi, S. Sathish, M. Abbas, V. Jeyakrishnan, R. Goel, et al., Peristaltic transport of Sutterby nanofluid flow in an inclined tapered channel with an artificial neural network model and biomedical engineering application, *Sci. Rep.*, **14** (2024), 555. https://doi.org/10.1038/s41598-023-49480-9
117. Amna, F. Aljuaydi, Z. Khan, S. Islam, Numerical investigations of ion slip and Hall effects on Cattaneo–Christov heat and mass fluxes in Darcy–Forchheimer flow of Casson fluid within a porous medium, utilizing non-Fourier double diffusion theories through artificial neural networks, *International Journal of Thermofluids*, **20** (2023), 100475. https://doi.org/10.1016/j.ijft.2023.100475
118. Z. Shah, M. Alhazmi, W. A. Khan, N. A. AlBasheir, R. Z. Haider, An artificial neural network approach to characterizing the behavior of bioconvective nanofluid model using backpropagation of Levenberg–Marquardt algorithm, *Int. J. Mod. Phys. B*, **39** (2025), 2540055. https://doi.org/10.1142/S0217979225400557
119. P. Kaswan, M. Kumar, M. Kumari, Analysis of a bioconvection flow of magnetocross nanofluid containing gyrotactic microorganisms with activation energy using an artificial neural network scheme, *Results in Engineering*, **17** (2023), 101015. https://doi.org/10.1016/j.rineng.2023.101015
120. M. Yaseen, S. K. Rawat, N. A. Shah, M. Kumar, S. M. Eldin, Ternary hybrid nanofluid flow containing gyrotactic microorganisms over three different geometries with Cattaneo–Christov model, *Mathematics*, **11** (2023), 1237. https://doi.org/10.3390/math11051237
121. Y. Qu, D. J. Jasim, S. M. Sajadi, S. Salahshour, A. Rahmanian, et al., Artificial neural network modeling of thermal characteristics of WO_3-CuO (50:50)/water hybrid nanofluid with a back-propagation algorithm, *Mater. Today Commun.*, **38** (2024), 108169. https://doi.org/10.1016/j.mtcomm.2024.108169
122. A. Borode, T. Tshephe, P. Olubambi, M. Sharifpur, J. Meyer, Effects of temperature and nanoparticle mixing ratio on the thermophysical properties of GNP-Fe_2O_3 hybrid nanofluids: an experimental study with RSM and ANN modeling, *J. Therm. Anal. Calorim.*, **149** (2024), 5059–5083. https://doi.org/10.1007/s10973-024-13029-3

123. S. K. Rawat, M. Yaseen, M. Pant, C. S. Ujarari, Designing artificial intelligence computing techniques to study heat transfer of a ternary hybrid nanofluid flow: application of particle swarm optimization and artificial neural network, *Mod. Phys. Lett. B*, **39** (2025), 2550114. https://doi.org/10.1142/S0217984925501143
124. S. Z. Cai, Z. P. Mao, Z. C. Wang, M. L. Yin, G. E. Karniadakis, Physics-informed neural networks (PINNs) for fluid mechanics: A review, *Acta Mech. Sin.*, **37** (2021), 1727–1738. https://doi.org/10.1007/s10409-021-01148-1
125. C. Zhao, F. F. Zhang, W. Q. Lou, X. Wang, J. Y. Yang, A comprehensive review of advances in physics-informed neural networks and their applications in complex fluid dynamics, *Phys. Fluids*, **36** (2024), 101301. https://doi.org/10.1063/5.0226562
126. Z. Y. Ren, S. J. Zhou, D. Liu, Q. H. Liu, Physics-informed neural networks: methodological evolution, theoretical foundations, and interdisciplinary frontiers toward next-generation scientific computing, *Appl. Sci.*, **15** (2025), 8092. https://doi.org/10.3390/app15148092
127. S. Goswami, A. Bora, Y. Yu, G. E. Karniadakis, Physics-informed deep neural operator networks, In: *Machine learning in modeling and simulation*, Cham: Springer, 2023, 219–254. https://doi.org/10.1007/978-3-031-36644-4_6
128. A. A. Howard, S. H. Murphy, S. E. Ahmed, P. Stinis, Stacked networks improve physics-informed training: applications to neural networks and deep operator networks, (2023), arXiv:2311.06483. https://doi.org/10.48550/arXiv.2311.06483
129. P. C. Meng, Z. B. Xu, X. C. Wang, W. S. Yin, H. Y. Liu, A novel method for solving the inverse spectral problem with incomplete data, *J. Comput. Appl. Math.*, **463** (2025), 116525. https://doi.org/10.1016/j.cam.2025.116525
130. J. B. Zhuang, P. C. Meng, W. S. Yin, A stable neural network for inverse scattering problems with contaminated data, *Knowl.-Based Syst.*, **310** (2025), 113001. https://doi.org/10.1016/j.knosys.2025.113001
131. Y. Xiao, Z. X. Jiang, P. C. Meng, W. S. Yin, D. Q. Qi, L. H. Zhou, Local manifold approximation of dynamical system based on neural ordinary differential equation, *Physica D*, **477** (2025), 134688. https://doi.org/10.1016/j.physd.2025.134688
132. P. Giudici, Safe machine learning, *Statistics*, **58** (2024), 473–477. https://doi.org/10.1080/02331888.2024.2361481

AIMS Press